JGR Solid Earth

RESEARCH ARTICLE

10.1029/2022JB025577

Jurassic Paleomagnetism of the Lhasa Terrane—Implications for Tethys Evolution and True Polar Wander

Yiming Ma[1,2,3], Qiang Wang[2,4,5], Huapei Wang[3], Bo Wan[6], Shihong Zhang[7], Chenglong Deng[6], Dongyu Zheng[8], Qiang Ren[8], Tianshui Yang[7], Dan Wu[1], Di Zou[1,3], Jun Wang[2], Xiao Liu[2,9], Zhiqiang Kang[9], Wei Dan[2,4], Fei Han[3], and Mark J. Dekkers[10]

[1]School of Earth Sciences, China University of Geosciences, Wuhan, China, [2]State Key Laboratory of Isotope Geochemistry, Guangzhou Institute of Geochemistry, Chinese Academy of Sciences, Guangzhou, China, [3]Paleomagnetism and Planetary Magnetism Laboratory, School of Geophysics and Geomatics, China University of Geosciences, Wuhan, China, [4]CAS Center for Excellence in Deep Earth Science, Guangzhou, China, [5]College of Earth and Planetary Sciences, University of Chinese Academy of Sciences, Beijing, China, [6]State Key Laboratory of Lithospheric Evolution, Institute of Geology and Geophysics, Chinese Academy of Sciences, Beijing, China, [7]State Key Laboratory of Biogeology and Environmental Geology, China University of Geosciences, Beijing, China, [8]State Key Laboratory of Oil and Gas Reservoir Geology and Exploitation & Institute of Sedimentary Geology, Chengdu University of Technology, Chengdu, China, [9]Guangxi Key Laboratory of Hidden Metallic Ore Deposits Exploration, College of Earth Sciences, Guilin University of Technology, Guilin, China, [10]Department of Earth Sciences, Utrecht University, Utrecht, The Netherlands

Key Points:

- The Lhasa terrane was located at ~8°S at ~180 Ma for the reference point (29.3°N, 90.3°E)
- Lhasa terrane's motion accelerated from ~2 cm/yr during ~220–180 Ma to ~17 cm/yr during ~180–170 Ma
- The Lhasa terrane underwent a yoyo-like drift motion near the equator at ~170–130 Ma, supporting the fast Late Jurassic true polar wander

Supporting Information:

Supporting Information may be found in the online version of this article.

Correspondence to:

Y. Ma,
maym@cug.edu.cn;
may.iming2006@163.com

Citation:

Ma, Y., Wang, Q., Wang, H., Wan, B., Zhang, S., Deng, C., et al. (2022). Jurassic paleomagnetism of the Lhasa terrane—Implications for Tethys evolution and true polar wander. *Journal of Geophysical Research: Solid Earth*, *127*, e2022JB025577. https://doi.org/10.1029/2022JB025577

Received 8 SEP 2022
Accepted 23 NOV 2022

Author Contributions:

Conceptualization: Yiming Ma, Qiang Wang, Huapei Wang, Bo Wan, Shihong Zhang, Chenglong Deng, Tianshui Yang, Dan Wu, Di Zou, Jun Wang, Xiao Liu, Zhiqiang Kang, Wei Dan, Fei Han, Mark J. Dekkers
Funding acquisition: Yiming Ma, Qiang Wang, Huapei Wang
Investigation: Yiming Ma, Qiang Wang, Huapei Wang, Dongyu Zheng, Qiang Ren, Tianshui Yang, Dan Wu, Di Zou, Jun Wang, Xiao Liu, Zhiqiang Kang, Mark J. Dekkers
Visualization: Yiming Ma, Qiang Wang, Bo Wan, Shihong Zhang, Dan Wu, Zhiqiang Kang, Wei Dan, Fei Han, Mark J. Dekkers
Writing – original draft: Yiming Ma, Tianshui Yang, Mark J. Dekkers

Abstract

The drift history of the Lhasa terrane from Gondwana to Asia plays a crucial role in understanding the Tethys evolution and true polar wander (TPW). However, few reliable paleomagnetic results from Jurassic strata are currently available for reconstructing its northward journey. We performed a combined paleomagnetic and geochronological study on Bima Formation strata in the Xigaze area. Combined with previous results from the Sangri area, our results reveal a paleolatitude of 8 ± 4°S at ~180 Ma for the reference point (29.3°N, 90.3°E). Along with other paleomagnetic results from the Triassic to Cretaceous, our new results suggest that the Lhasa terrane motion accelerated from ~2 cm/yr during ~220–180 Ma to ~17 cm/yr during ~180–170 Ma. Paleolatitude information of the North Qiangtang terrane and Tethyan Himalaya is calculated from paleopoles that meet five criteria, which include (a) structural control, (b) well-determined rock age, (c) stepwise demagnetizations, (d) a minimum of 25 specimens or 8 sites are contained, and (e) robust field or reversal tests are provided. Both terranes also show significant acceleration during their northward motion, which may be related to oceanic slab subduction. Thus, all Gondwana-derived microcontinents seem to share a significant acceleration during their northward motion. In addition, recent paleomagnetic results from volcanic rocks dated at ~155 Ma subdivide the overall northward motion during ~170–130 Ma into two stages, which include a southward drift during ~170–155 Ma followed by northward motion during ~155–130 Ma. These results support the fast Late Jurassic TPW during a ~10 Myr time span.

Plain Language Summary

The Tibetan Plateau is composed of the Qiangtang, Lhasa, and Himalaya terranes that originate from Gondwana, which was an ancient supercontinent located mainly in the southern hemisphere. How these terranes moved northward from Gondwana to Asia remains unclear due to poor paleolatitude constraints. We provide paleomagnetic evidence to show that the Lhasa terrane was located at ~8°S at ~180 million years ago (Ma). Together with reliable paleomagnetic data from Late Triassic (~237–201 Ma) limestones and Middle Jurassic (~174–163 Ma) sandstones, our results suggest a significant acceleration during Lhasa's northward motion at ~220–170 Ma. Reliable paleolatitude data show significant accelerations of the Lhasa, North Qiangtang, and Tethyan Himalaya terranes during their northward journey, which may be related to oceanic slab subduction. These significant accelerations may be a common feature of these Gondwana-derived microcontinents. The drift history of the Lhasa terrane during ~170–130 Ma can be subdivided into a southward drift during ~170–155 Ma and a subsequent northward drift during ~155–130 Ma. The yoyo-like drift motion of the Lhasa terrane near the equator before and after ~155 Ma supports a fast Late Jurassic pole motion event (named true polar wander) during a ~10 Myr time span.

1. Introduction

The opening and closure of the Paleo-Tethys and Neo-Tethys—the latter includes the Meso-Tethys and Ceno-Tethys (Metcalfe, 2021) — during the Phanerozoic are determined by the behavior of four continental slivers, which

10.1029/2022JB025577

Writing – review & editing: Yiming Ma, Qiang Wang, Huapei Wang, Shihong Zhang, Chenglong Deng, Qiang Ren, Tianshui Yang, Dan Wu, Wei Dan, Fei Han, Mark J. Dekkers

include and are represented by the North Qiangtang, South Qiangtang, Lhasa, and Himalaya terranes within the Tibetan Plateau (Figure 1). This slivers' evolution involves their breakup from Gondwana and the subsequent northward motion until the final accretion to Asia. The Meso-Tethys opened between the Cimmeride terranes and Gondwana in the Permian; it closed in the Late Jurassic-Cretaceous (Y. Ma et al., 2018; Metcalfe, 2021; Wei et al., 2022). The Cimmeride terranes included the South Qiangtang and Sibumasu terranes in the east, and Iran, Afghanistan, and other terranes in the west (X. D. Wang et al., 2021; Wei et al., 2022) (Figure 1a). They accreted onto the southern margin of Asia in the Triassic, marking the closure of the Paleo-Tethys (Metcalfe, 2021). The Ceno-Tethys opened in the Triassic-Jurassic, which separated the Lhasa terrane and East Java–West Sulawesi from the India-Australian margin of Gondwana (Metcalfe, 2021). The India-Asia collision in the Paleocene-Eocene marked the closure of the Ceno-Tethys (Hu et al., 2016; Yang et al., 2019). The closure of the Tethys marked by several suture zones led to the formation of the Tibetan Plateau, influencing the regional and even global climate (Yin & Harrison, 2000) (Figure 1). Because the Tethys seafloor has entirely been subducted, the evolution of the Tethys oceanic crust can only be reconstructed by the tectonic evolution of adjacent diverging plates (Matthews et al., 2016).

The Tibetan Plateau is surrounded by the Tarim Block, the North China Block, the South China Block, and the Indian Craton (Figure 1a). It is a geological amalgamation that consists of the afore-mentioned series of Gondwana-derived microcontinents that sutured with Asia one by one during the Phanerozoic (An et al., 2021; Dewey et al., 1988; Ding et al., 2013; Ma et al., 2018; Yan et al., 2016; Yi et al., 2021; Zhu et al., 2016), making it one of the best areas to unravel the evolution of the Tethys realm (Figure 1b).

The Lhasa terrane is bounded by the Bangong-Nujiang suture zone (Meso-Tethys) to the north and by the Yarlung Zangbo suture zone (Ceno-Tethys) to the south (Figure 1b). The long northward journey of the Lhasa terrane, from Gondwana to Eurasia, makes paleomagnetism a critical method to reconstruct its rift-and-drift history and, alongside, the plate tectonic evolution of the Tethys oceanic crust (Li et al., 2016; Ma et al., 2014). Previous paleomagnetic investigations mainly focused on the Cretaceous–Eocene to constrain the India–Asia collision and intracontinental deformation within Asia, revealing that the Lhasa terrane was located at a stable northern hemisphere latitude from the Cretaceous until the India-Asia collision (Bian et al., 2017, 2020; Cao et al., 2017; Chen et al., 2012; Dupont-Nivet et al., 2010; van Hinsbergen et al., 2012; Huang, van Hinsbergen, Maffione, et al., 2015; Huang, van Hinsbergen, Lippert et al., 2015; Li et al., 2017; Liebke et al., 2010; Lippert et al., 2014; Ma et al., 2014, 2017, 2018; Ma, Wang, et al., 2022; Ma, Yuan, et al., 2022; Meng et al., 2012; Sun et al., 2010, 2012; Tan et al., 2010; Tang et al., 2013; Tong et al., 2017, 2019; S. Wang et al., 2022; Yang, Ma, Zhang, et al., 2015; Yi et al., 2015). In addition, Zhou et al. (2016) obtained a stable southern hemisphere latitude for the Triassic from the Coqen limestones. However, how the Lhasa terrane moved northward from Gondwana to Asia remains unclear, making the Jurassic a critical period for constraining the northward drift from Gondwana to Asia.

Notably, available results from the North Qiangtang terrane and Tethyan Himalaya seem to suggest that these two terranes had significant accelerations during their northward movement from Gondwana to Asia (Guan et al., 2021; van Hinsbergen et al., 2012; Ma et al., 2019; Song et al., 2015, 2017; Yu et al., 2022; Yuan et al., 2021, 2022). Conrad and Lithgow-Bertelloni (2002) suggested that the gravitational pull of subducted slab is an essential driving force of plate motion, which may lead to an acceleration of the subducting plate (Sun, Liu, et al., 2018). However, it remains unclear whether the Lhasa terrane also experienced acceleration during the Jurassic. Recently, Li et al. (2022) reported new paleomagnetic results with positive fold and reversal tests from well-dated Late Jurassic lava flows, revealing a similar near-equatorial paleolatitude at ~155 Ma and ~180 Ma (Li et al., 2016). These observations are inconsistent with the northward motion of the plates, let alone the acceleration of the Lhasa terrane during the Jurassic (Li et al., 2016; Ma et al., 2014; Zhou et al., 2016). Therefore, Li et al. (2022) suggested that the seeming stand-still was due to Jurassic true polar wander (TPW). Although different Jurassic TPW models suggest a similar total rotational amplitude, the presence of the Late Jurassic monster shift is under debate (Fu et al., 2020; Kent & Irving, 2010; Torsvik et al., 2012). Based on the paleolatitude evolution of the Lhasa terrane, Li et al. (2022) were unable to confirm or reject the existence of a short-lived latest Jurassic-earliest Cretaceous TPW event.

A well-constrained Jurassic drift history of the Lhasa terrane enables us to explore this issue further. However, too few Jurassic data with exact age constraints are available to determine a potential velocity change of the Lhasa terrane during its translocation from Gondwana to Asia. Furthermore, no reliable Jurassic paleomagnetic results

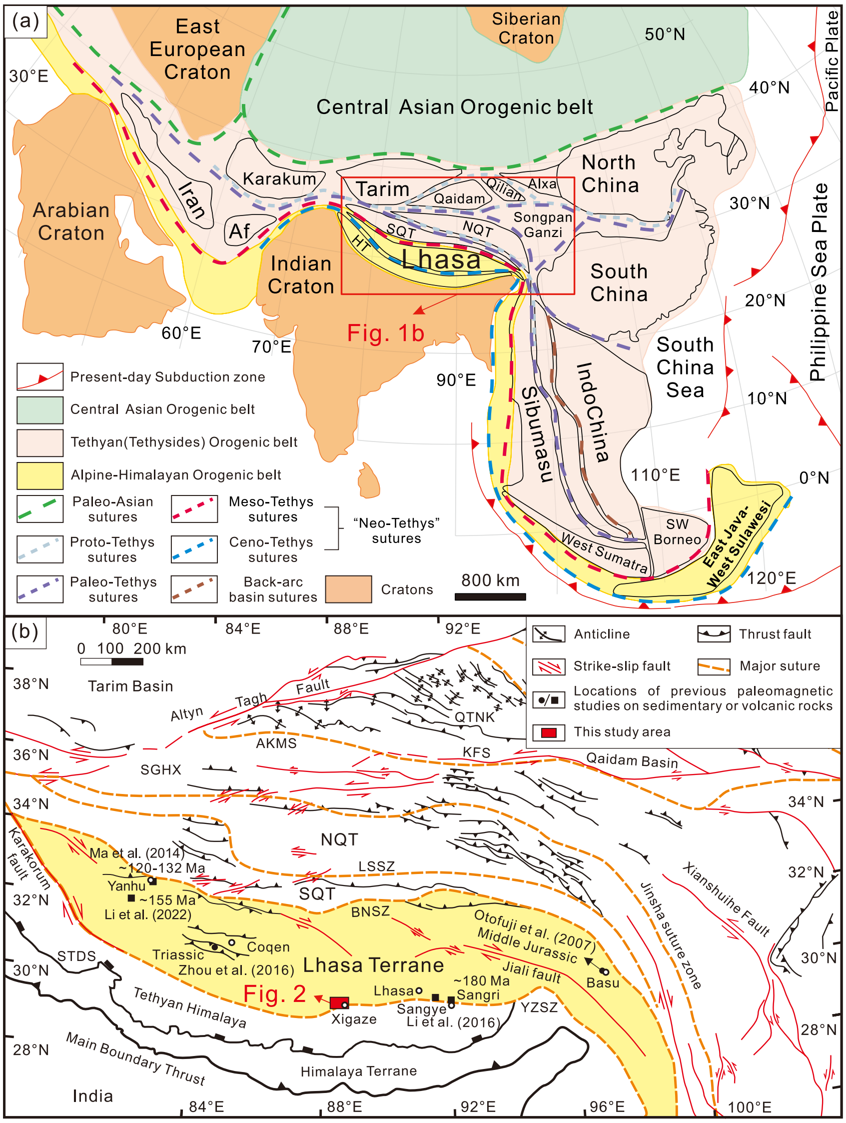

Figure 1. (a and b) The major orogenic belts of Asia and regional tectonic map of the Tibetan Plateau and adjacent areas, modified from Metcalfe (2021) and Yin and Harrison (2000), respectively. Abbreviations: Af, Afghanistan; AKMS, Ayimaqin-Kunlun-Muztagh suture zone; BNSZ, Bangong-Nujiang suture zone; KFS, Kunlun fault system; LSSZ, Longmuco-Shuanghu suture zone; NQT, North Qiangtang terrane; QTNK, Qimen Tagh-North Kunlun thrust system; SGHX, Songpan-Ganzi-Hoh Xil terrane; SQT, South Qiangtang terrane; STDS, South Tibet detachment system, which separates the Tethyan Himalaya from other parts of the Himalaya terrane; HT, Himalaya terrane; YZSZ, Yarlung Zangbo suture zone.

are available from the mid-western part of the 2,500 km-long Lhasa terrane. Therefore, we performed a combined paleomagnetic and geochronological study on the Jurassic volcano-sedimentary sequence of the Bima Formation near Xigaze city to constrain the Lhasa terrane's drift history.

2. Geology and Sampling

Lhasa terrane's southern part is characterized by widespread Mesozoic-Cenozoic Gangdese batholiths and their eruptive equivalents, ranging in age from the Triassic to the Neogene (Sundell et al., 2021; C. Wang et al., 2016). The Sangri Group, with the Mamuxia Formation making up its lower part and the Bima Formation its upper part, is unconformably overlain by the Late Cretaceous Danshiting Formation, indicating that the folding of the Bima Formation is not post-dating the Danshiting Formation (~90–97 Ma) (Ran et al., 2019). The volcano-sedimentary sequence of the Bima Formation is sporadically exposed along the Lhasa terrane's southern margin from 85°E

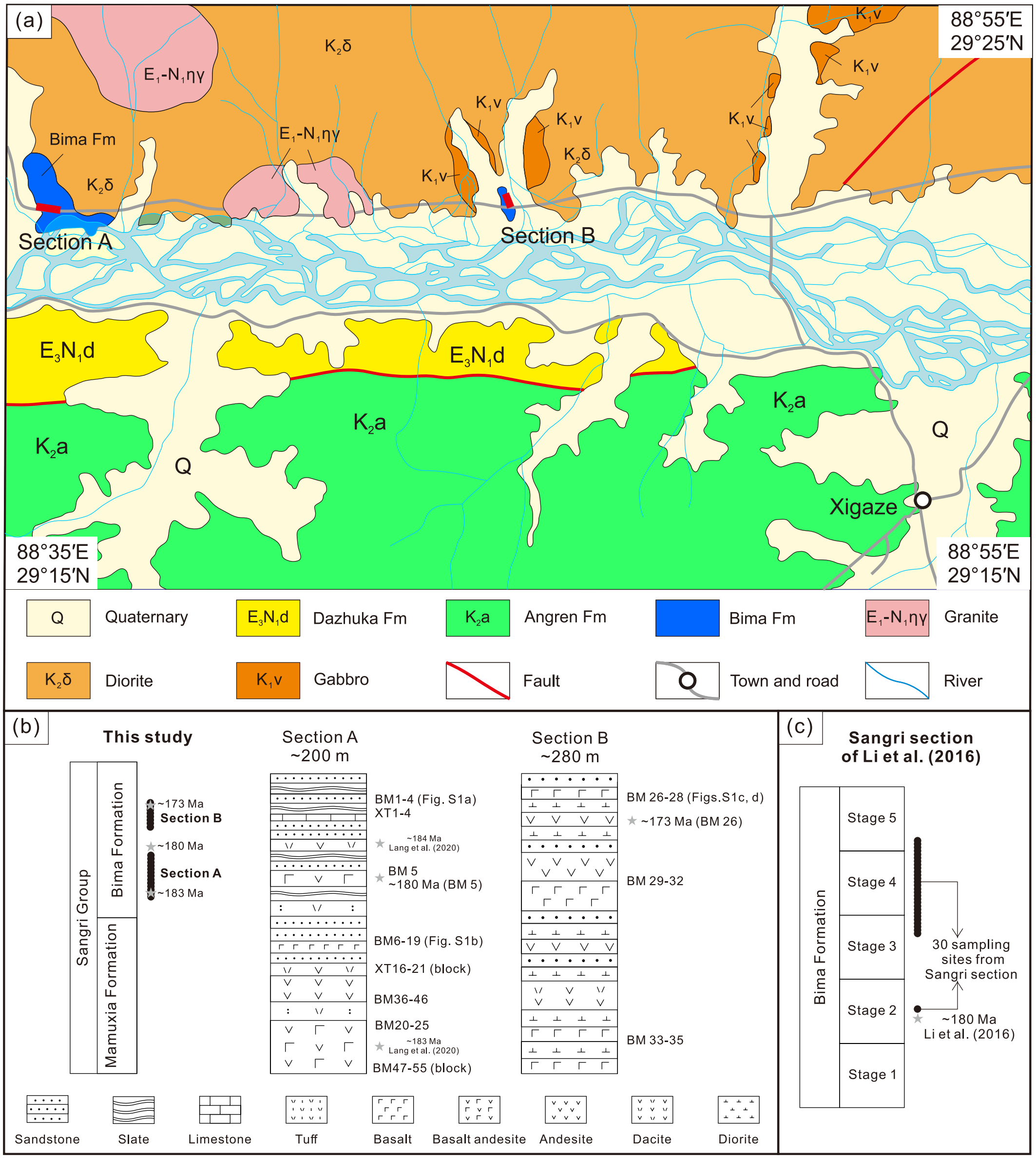

Figure 2. (a) Simplified geologic map of the sampling region of this study (after Hu et al., 2014). (b) The stratigraphic column of the Bima Formation of the Sangri Group showing the sampling units of this study. Section A is modified from Lang et al. (2020) and includes our field observations; Section B is based on our field observations. (c) The five stages of the Bima Formation of the Sangri Group showing the sampling interval of Li et al. (2016). Five stages are distinguished in the Bima Formation based on Kang et al. (2014). Age comparison between this study and Li et al. (2016) reveals that the age of sampling sites BM6-55 from section A in this study is older than that of the sites in the Sangri section of Li et al. (2016).

to 92°E (Figures 1 and 2) (X. L. Chen et al., 2019). It is mainly composed of basalt, basaltic andesite, andesite, and dacite, interbedded with limestone, sandstone, and siltstone (Hu et al., 2014; Kang et al., 2014; Lang et al., 2020). The Bima Formation in the southern margin of Asia is often mapped as being Early Cretaceous in age; however, recent radiometric dating of the volcanic shows that they formed during the Early to Middle Jurassic (~195-165 Ma) (X. L. Chen et al., 2019; Kang et al., 2014). The southern margin of the Lhasa terrane was massively intruded, leading to an intrusive contact between the Bima Formation and the Cretaceous intrusive rocks in the Xigaze area (Figure 2a). Although the soft layers of the Bima Formation have suffered from deformation (Figure S1a of Supporting Information S1), the competent layers, including sandstone and volcanic, maintain their original structure and have not suffered from significant deformation and metamorphism (Lang et al., 2020; Ran et al., 2017) (Figure S1 of Supporting Information S1).

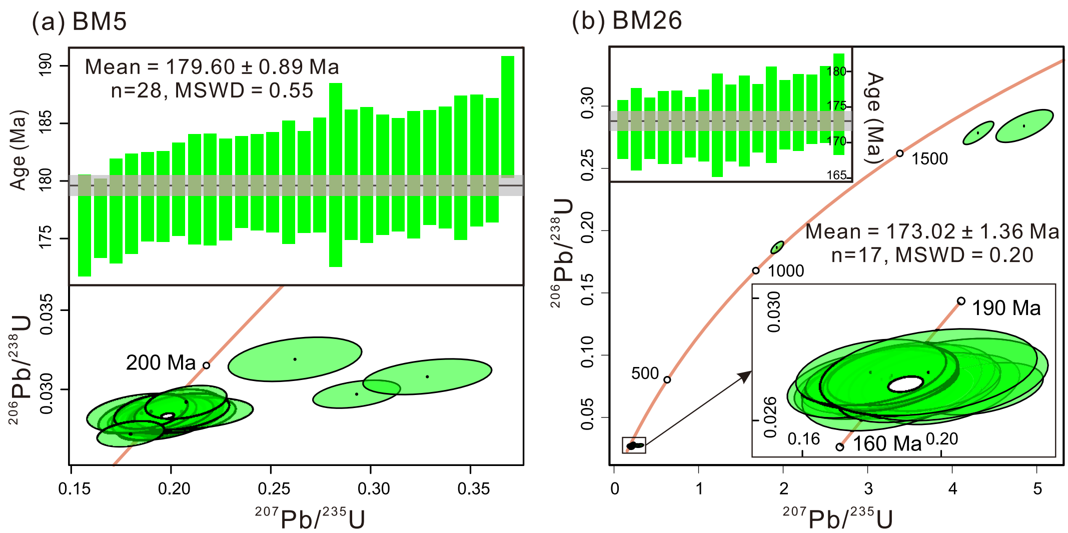

Figure 3. (a and b) Concordia diagrams showing $^{206}Pb/^{238}U$ ratios and weighted mean of apparent $^{206}Pb/^{238}U$ ages of zircon grains in samples BM5 and BM26.

We collected 349 paleomagnetic cores from 40 sites and 27 oriented block samples from section A (29.36°N, 88.59°E) and 87 cores from 10 sites from section B (29.37°N, 88.74°E) of the Bima Formation volcano-sedimentary sequence in the Xigaze area (Figure 2). The bottom and top of the Bima Formation strata are not exposed in our two sampling sections. Both sections show evident bedding attitudes (Figure S1 of Supporting Information S1). Two fresh block samples near paleomagnetic sites BM5 and BM26 from Sections A and B, respectively, were sampled for zircon U–Pb dating. Detailed methods, laboratory techniques, and measurements are provided in Text S1 in the Supporting Information S1.

3. Results

3.1. Zircon U–Pb Geochronology

Most zircon grains are euhedral to subhedral, showing clear banded zoning in cathodoluminescence (Figure S2 of Supporting Information S1). All 32 analyses from BM5 yield similar $^{206}Pb/^{238}U$ ages, with 29 falling on the concordance line (Figure 3a). One zircon age is neglected here because it is far away from the weighted mean $^{206}Pb/^{238}U$ ages of the youngest group (Table S1). The remaining 28 zircon ages have their weighted mean intersecting within their individual confidence limit (Figure 3a). Three analyses do not fall on the concordance line, likely due to the existence of a minor amount of common lead (Figure 3a). These 28 zircons with consistent $^{206}Pb/^{238}U$ ages yield a weighted mean of 179.6 ± 0.9 Ma (Figure 3a).

Twenty-nine analyses from BM26 yield three age groups, with the youngest age group composed of 17 grains falling on the concordance line (Figure 3b; Table S1). These grains yield a weighted mean $^{206}Pb/^{238}U$ ages of 173.0 ± 1.4 Ma (Figure 3b). The age range of ~180-173 Ma is interpreted as the emplacement age of the studied Bima volcanic rocks, which is consistent with the ~195-165 Ma range reported by previous studies (X. L. Chen et al., 2019; Kang et al., 2014; Lang et al., 2020). The age of the sampled Bima Formation in this study is consistent with that of Li et al. (2016) (Figures 2b and 2c).

3.2. Rock Magnetic Analyses

Eighteen specimens were chosen for rock magnetic analyses. The acquisition curves of the isothermal remanent magnetization (IRM) of two specimens exhibit a rapid increase below 300 mT, and saturation IRM (SIRM) is not entirely reached even at 1 T (Figures 4a and 4b). These results, together with component analysis of the IRM (Figures S3a and S3b of Supporting Information S1), the coercivity of remanence of ~160 mT (Figure 4a), and the unclosed hysteresis loops at ~1 T (Figure S4b of Supporting Information S1), show the existence of different coercivity magnetic carriers. The κ-T curve of one specimen is barely interpretable due to low signal-to-noise

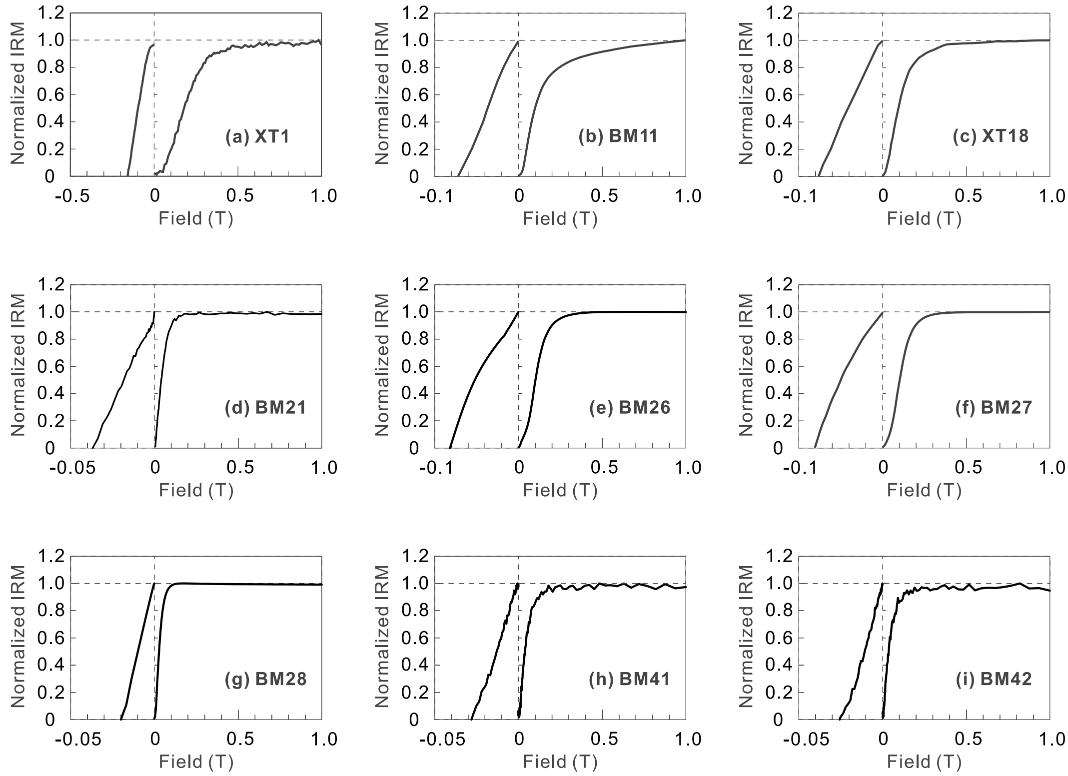

Figure 4. Isothermal remanent magnetization (IRM) acquisition and back-field demagnetization curves of the saturation IRM of representative specimens of the Bima Formation.

ratios (Figure 5a). Another specimen shows a distinct increase after heating to 225°C and a significant drop before ~330°C, implying the existence of pyrrhotite in this specimen (Figure 5b). A decrease in magnetic susceptibility near 580°C points to the existence of magnetite. Due to scattered demagnetization diagrams, no reliable remanence directions could be determined from these two specimens. Therefore, these specimens were neglected in further analyses.

The IRM acquisition curves of the remaining 16 specimens show a rapid increase below 200 mT, with the SIRM being almost achieved at 600 mT (Figures 4c–4i). The maximum and average remanent acquisition coercive forces (B_{cr}) of these specimens are 82.9 and 43.6 mT, respectively, revealing the existence of low-coercivity magnetic carriers (Figures 4c–4i). The component analyses of the IRM show that the low-coercivity components 1 and 2 with $B_{1/2}$ (the field when half of SIRM is acquired) of ~11–110 mT contribute ~81–100% to the SIRM, while the high-coercivity component 3 with $B_{1/2}$ of 157.7–348.9 mT contributes 7.1%–19.0% to the SIRM, indicating the dominance of the low-coercivity magnetic carriers in these specimens (Figures S3c-i of Supporting Information S1) and a minor contribution of high-coercivity carriers in some specimens (Figures S3c and S3e of Supporting Information S1). The narrow hysteresis loops of these specimens show a pseudo-single-domain-like shape, supporting the dominance of the low-coercivity magnetic carriers (Figures S4c-i of Supporting Information S1). The significant drop in susceptibility at ~580°C indicates that the low-coercivity magnetic carriers are magnetite (Figures 5c–5i). The susceptibility markedly increased during 100–300°C, suggesting a change in the magnetic phase during heating (Figures 5e–5g). These 16 samples plot in the pseudo-single-domain region of the Day plot (Day et al., 1977; Dunlop, 2002) (Figure S5 of Supporting Information S1), generally following the SD and multidomain (MD) mixing curves, indicating SD and MD mixtures (Dunlop, 2002) or a stable vortex state (Roberts et al., 2017) for the magnetite of these representative samples. These 16 specimens belong to volcanic rocks, as indicated by their typical porphyritic texture (e.g., XT18 shown in Figure 6b) and homogeneous structure. The Fe oxide content in the volcanic sites of Section A is much lower than that in Section B, leading to a much lower susceptibility in Section A (Figures 5a–5d, 5h and 5i) than in Section B (Figures 5e–5g). Nevertheless, meaningful characteristic remanent magnetizations (ChRMs) can be determined from volcanic rocks in both sections. We perform petrographic observations on four of these specimens.

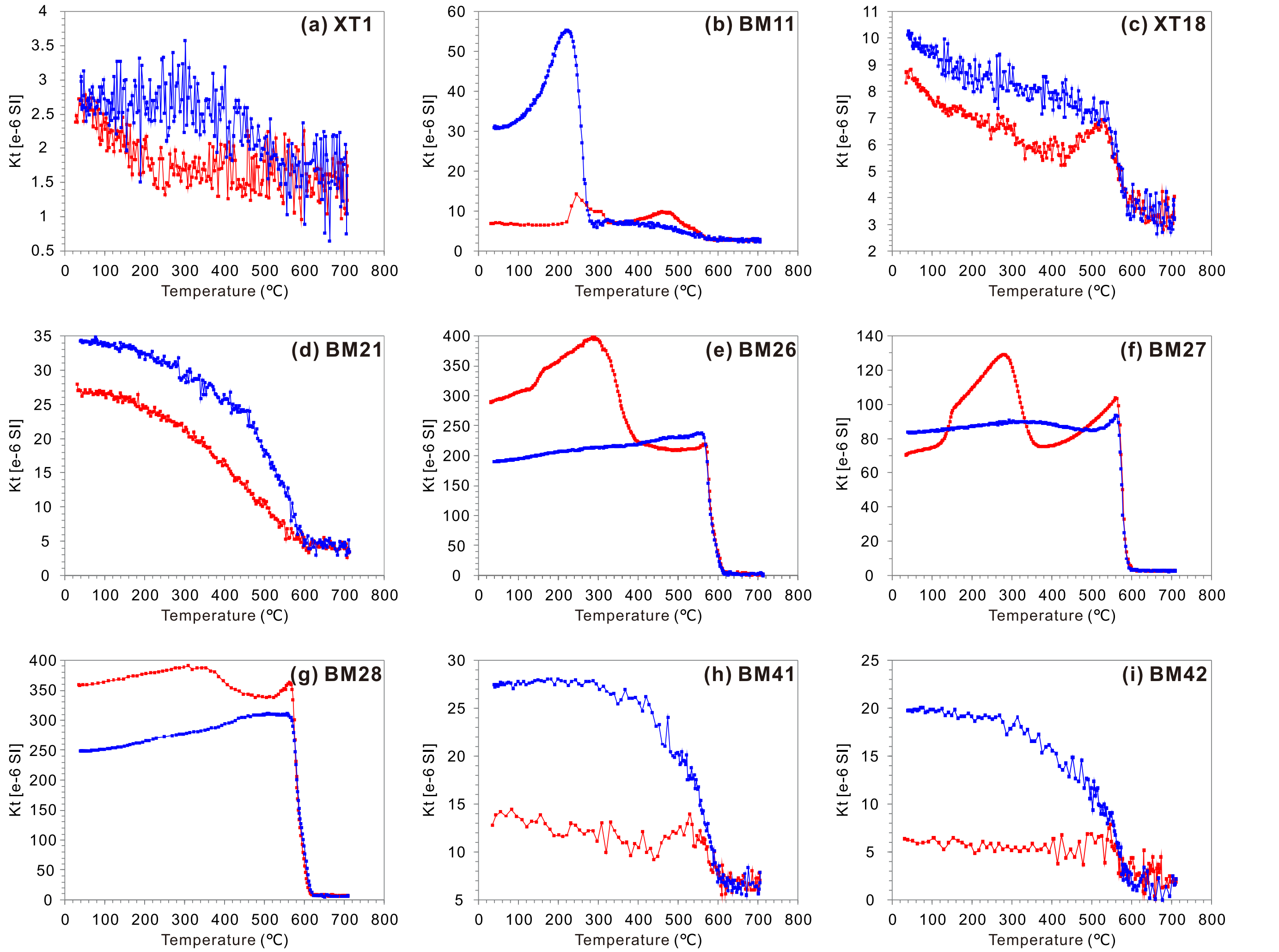

Figure 5. Susceptibility versus temperature (κ-T) curves of representative Bima Formation specimens (same samples as Figure 4). The heating (cooling) curves are in red (blue).

3.3. Petrographic and Paleomagnetic Analyses

Magnetic petrographic observations of these specimens further support our rock magnetic interpretation. The energy-dispersive microprobe analyses reveal abundant Fe oxide grains in our specimens. These Fe oxide grains show irregular to euhedral shapes with various sizes ranging from less than 10 μm for most grains to more than 30–100 μm for some grains, indicating a typical magmatic origin of magnetite and titanomagnetite (Figure 6). The grain sizes of the Fe oxides are consistent with the SD and MD mixtures in these representative samples.

A reliable ChRM is isolated in 124 specimens (Figure 7). For these specimens, a low-temperature component is isolated between ~100°C and ~250°C in thermal demagnetization in 86 specimens (Figure S6 of Supporting Information S1). It has a downward, northerly direction in in-situ coordinates, implying a viscous origin of the present geomagnetic field (Figure 7 and Figure S6 of Supporting Information S1). The low-temperature component directions are followed by intermediate-temperature component directions determined between ~300°C and ~450°C in 50 specimens (Figure 7 and Figure S7 of Supporting Information S1). The intermediate-temperature component directions are nearly antipodal with the high-temperature component (HTC) directions (Figure S7 of Supporting Information S1 and Figures 8a and 8b). The intermediate-temperature component of these specimens may be caused by a potential self-reversal magnetization, which is due to magnetostatic interaction as a result of the presence of at least two magnetic phases having different unblocking temperatures (Krása et al., 2005; Liebke et al., 2012). Two magnetic phases with distinct unblocking temperatures fit well with the different Ti contents of

10.1029/2022JB025577

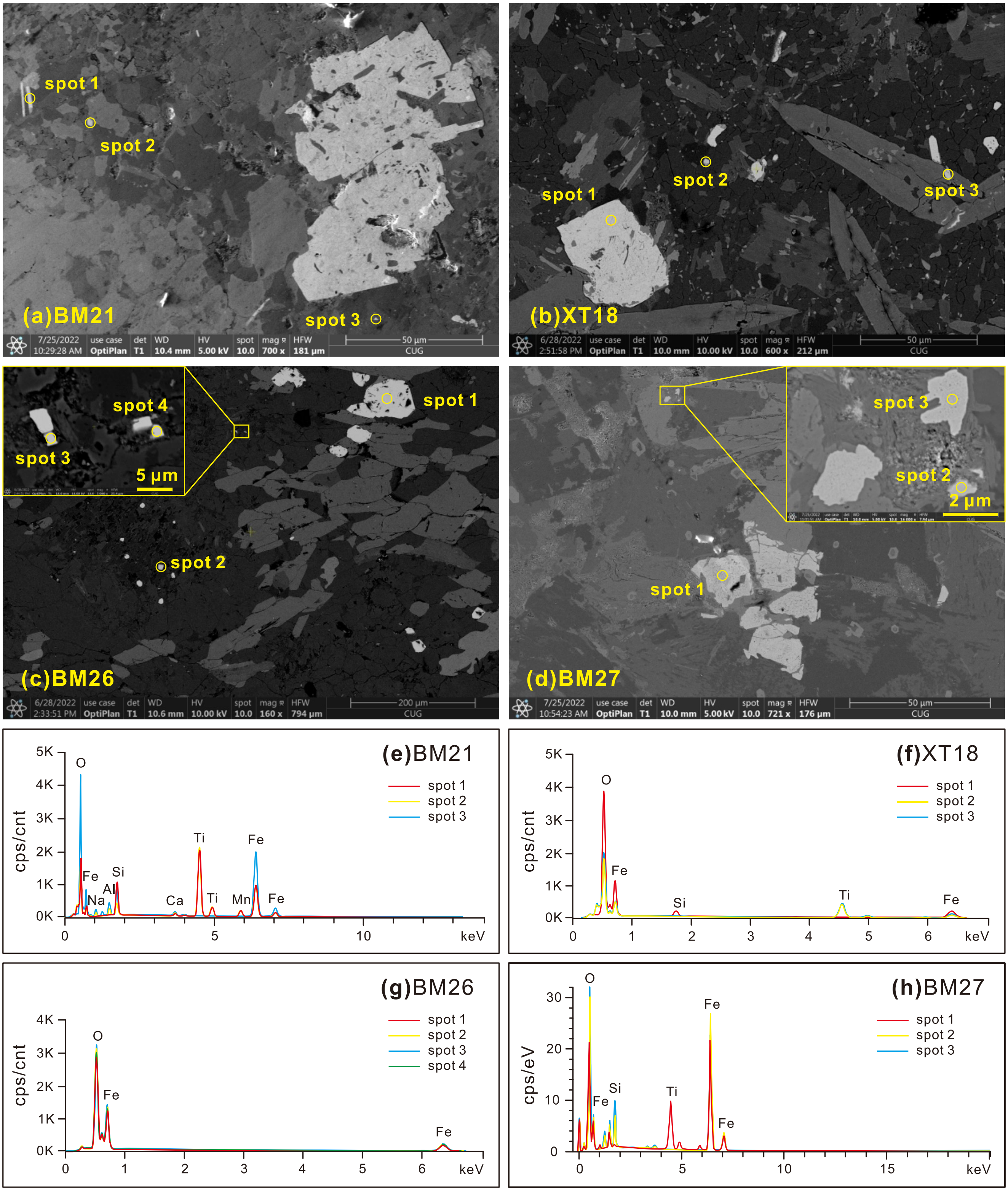

Figure 6. Scanning electron microscopy (SEM) micrographs (a–d) and energy dispersive spectra (e–h) of typical specimens. The open circles in (a–d) indicate the spots of the energy dispersive spectrometer (EDS) analyses. (e–g) are measured with an Oxford SDD Inca X-Max 50 EDS; (h) is measured with an EDAX EDS system (see Text S1 for more detail).

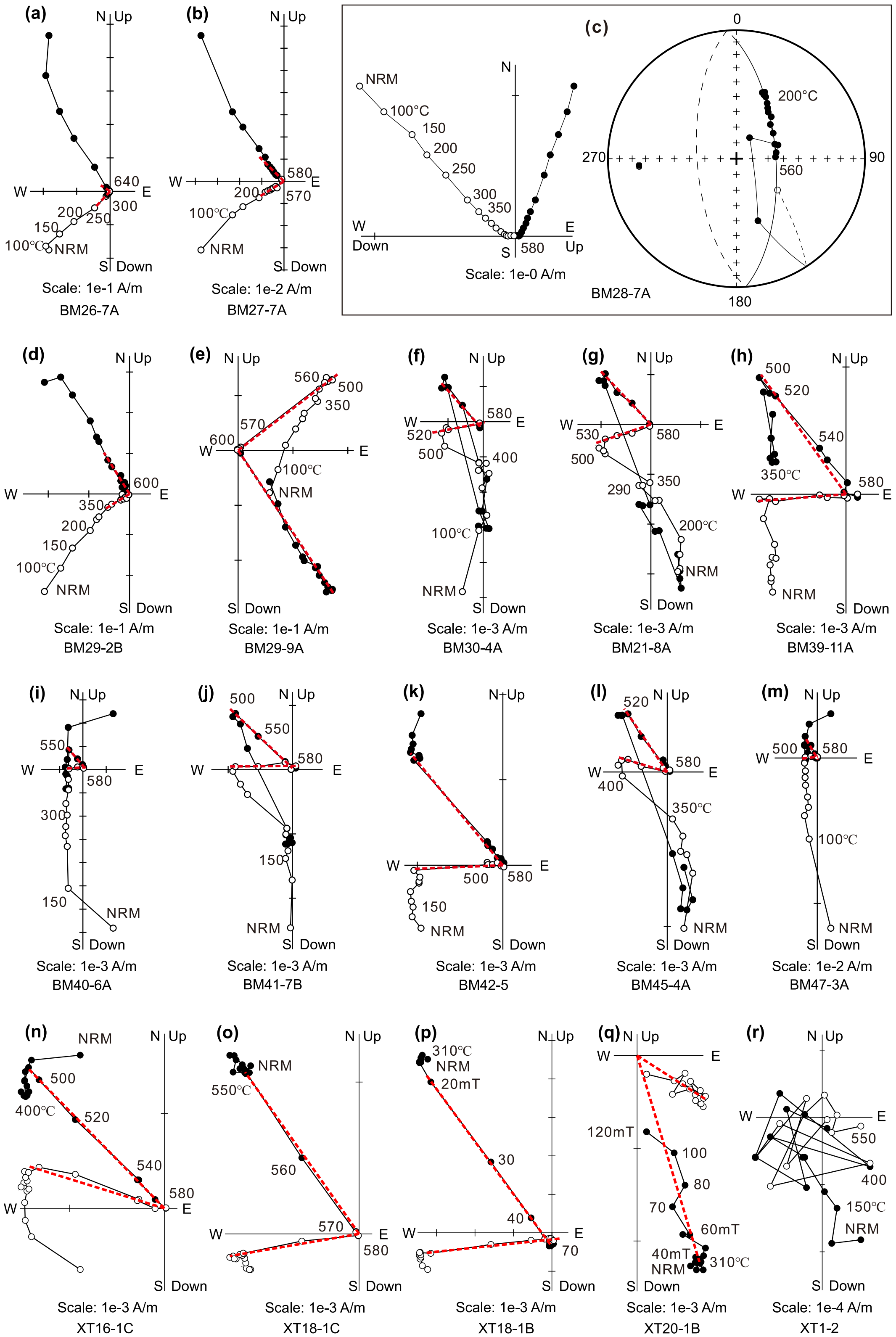

Figure 7. Demagnetization diagrams of representative specimens from Section B (a-f) and Section A (g-r) in geographic coordinates. The solid (open) symbols represent projections onto horizontal (vertical) planes; (c) shows the remagnetization great circle planes of BM28-7A; (r) shows an example of a scattered demagnetization diagram that is not considered further.

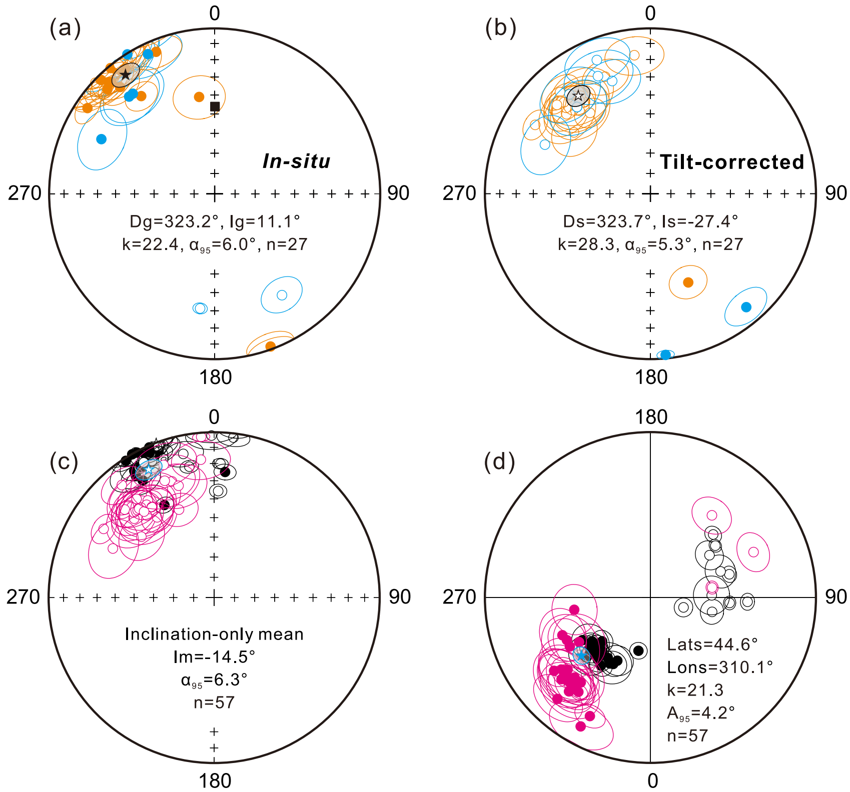

Figure 8. (a and b) Equal-area projections of site-mean ChRM directions of the Bima Formation volcanic rocks of this study. The orange and cyan circles are the results from Sections A and B, respectively. The black square indicates the present-day field direction ($D = 0.2°$, $I = 46.2°$) in the in-situ coordinates panel; (c and d) Equal-area projections of 57 sites ChRM directions from the Bima Formation volcanic rocks and corresponding VGPs (Table S6). Red and black circles are results from this study and Li et al. (2016), respectively. All 57 ChRM directions are shown as normal polarity to ease comparison. The stars indicate the overall mean of 27 sites for (a) and (b) and 57 sites for (c) and (d). Open (solid) circles are directions or VGPs in the upper (lower) hemisphere.

Fe oxides of various sizes (Figure 6). The magnetic phases with higher Curie temperatures may record a stable remanence in the direction of the paleomagnetic field (Krása et al., 2005). Therefore, we only consider the HTC as a potential primary natural remanent magnetization (NRM) in further analyses.

Stable HTCs decaying toward the origin is isolated between ∼500°C and ∼580°C in thermal demagnetization using the principal component analysis described in Kirschvink (1980) (Figure 7). Rock magnetism and magnetic petrography reveal that the ChRM directions are residing in magnetite and titanomagnetite, which is consistent with the maximum unblocking temperature at ∼580°C. The sizes of the (titano-) magnetite, as small as several micrometers, support their ability to record a primary NRM, as previous studies have shown (e.g., Ma et al., 2014, 2019).

The ChRMs can also be isolated by AF demagnetization between ∼20 and ∼100 mT (Table S2; Figure 7p). The ChRM directions for parallel samples from a single core isolated by the two different methods are compatible, testifying to their effectiveness and arguing for interpreting the ChRM as geologically meaningful (Figures 7o and 7p). The ChRM is thus recorded by low-coercivity magnetic carriers but not high-coercivity carriers. The HTCs mainly reside in (titano-) magnetite. The ChRM directions of 124 specimens, with maximum and average maximum angular deviation values of 15° and 7.6°, respectively, are used in further analyses (Table S2). Due to low NRM intensity or unstable magnetic carriers, many samples did not deliver a reliable ChRM direction. Some specimens show deviating remanence directions with a great circle tendency in their demagnetization diagrams, indicating potential remagnetizations (Figure 7c). Therefore, remagnetization great circle fitting was used to determine the ChRM directions of 14 specimens (Table S2) (McFadden & McElhinny, 1988).

The ChRM directions of 138 specimens distributed over 27 sites are listed in Table S2. The in-situ site-mean direction of the 27 sites is Dg = 323.2°, Ig = 11.1°, k = 22.4, and α_{95} = 6.0° while the grand mean after tilt correction is Ds = 323.7°, Is = −27.4°, k = 28.3, and α_{95} = 5.3° (Figures 8a and 8b; Table 1). The McFadden (1990) fold test shows that the statistical parameters for the mean direction are $\xi_{1,g}$ = 6.68 and $\xi_{2,g}$ = 8.58 in situ and $\xi_{1,s}$ = 5.42 and $\xi_{2,s}$ = 1.26 after tilt correction, respectively. The critical values at the 95% and 99% confidence levels are 6.04 and 8.55, respectively, revealing a positive McFadden (1990) fold test at the 99% confidence level. The positive fold test suggests that the remanence recorded by the Bima volcanic rocks is acquired before folding, which is before ~97 Ma (Ran et al., 2019). Because the Late Cretaceous diorites were dated at ~73–95 Ma (Hu et al., 2014), the remanence recorded by our samples is not influenced by this later intrusive activity. Only three sites show reverse polarity, which may be due to the intermittent volcanic activity and the discontinuous outcrop. Nevertheless, the antipodal dual-polarity directions pass the reversal test at the 95% confidence level (McFadden & McElhinny, 1990). These results show that the ChRMs recorded by the volcanic rocks are primary (Meert et al., 2020).

The tilt-corrected site-mean direction of eight sites from section B is Ds = 328.8°, Is = −21.6°, k = 17.0, and α_{95} = 13.8°, which share a common true mean direction with that of 19 sites from section A: Ds = 321.4°, Is = −29.7°, k = 43.3, and α_{95} = 5.2° (McFadden & McElhinny, 1990) (Table 1). The A_{95} values of the paleopoles of Sections A and B are 5.0° and 13.0°, respectively, which fit well with the *N*-dependent confidence intervals (3.7°, 12.8°) and (5.2°, 22.1°), respectively, implying that the confidence limit of the paleopole is consistent with field variability due to paleosecular variation (Deenen et al., 2011). The paleopoles yield corresponding paleolatitudes of 16 ± 5°S at ~180–183 Ma for Section A and 11 ± 13°S at ~173 Ma for Section B. The different paleolatitudes for Sections A and B may be due to the northward movement of the Lhasa terrane or an insufficient averaging of paleomagnetic field secular variation. Given that the A_{95} of section B paleopoles is too large for estimating the paleolatitude and that the remanence directions of the overall 27 sites from two sections are fully intersectional within the 95% confidence limit (Figure 8b), we only use the overall 27 sites of ~173–183 Ma in the following analyses (Lang et al., 2020; Figure 2b).

The site-mean paleopole of 27 sites is located at 33.5°N, 312.3°E, with K = 31.9 and A_{95} = 5.0° (Table 1), yielding a paleolatitude of 15 ± 5°S for the Xigaze area (29.4°N, 88.6°E). The A_{95} values fall within the *N*-dependent confidence interval (3.2°, 10.3°), implying that the confidence limit of the paleopole is consistent with paleosecular variation (Deenen et al., 2011). The new pole fulfills all the 7-point data quality criteria proposed by Van derVoo (1990) and updated by Meert et al. (2020), including (a) well-dated rock age within ±15 Ma; (b) stepwise demagnetization by multiple methods and tests for averaging of the paleosecular variation; (c) rock magnetic and microscopic examination and identification of magnetic carriers; (d) field test that constrain the age of magnetization; (e) structural control and tectonic coherence with block; (f) presence of reversal; (g) a lack of resemblance to younger poles.

Because volcanic rocks can only provide spot readings of the paleomagnetic field, averaging the paleosecular variation is essential for meaningful tectonic reconstructions based on a volcanic dataset. Some researchers suggest that some stratigraphically adjacent sites with the same ChRM direction (a shared common true mean direction) sample the same spot reading of the field and should count as one reading to better average the paleosecular variations (e.g., Chenet et al., 2008; Lippert et al., 2011, 2014). The common true mean direction test described by McFadden and McElhinny (1990) is typically used to identify whether two successive sites have identical ChRM directions. Fifteen independent directional groups were discerned from the 27 site mean directions by the common true mean direction test (Table S3). The in-situ group-mean direction of the 15 groups is Dg = 324.9°, Ig = 14.9°, k = 15.4, and α_{95} = 10.1° while the grand mean after tilt correction is Ds = 325.5°, Is = −26.3°, k = 18.6, and α_{95} = 9.1° (Table S3), yielding a paleopole located at 35.0°N, 311.1°E, with K = 20.7, and A_{95} = 8.6°, corresponding to a paleolatitude of 14 ± 9°S for the Xigaze area (29.4°N, 88.6°E). The A_{95} values fall within the N-dependent confidence interval (4.1°, 14.9°), implying that the confidence limit of the paleopole is consistent with the secular variation of the paleomagnetic field (Deenen et al., 2011). Notably, due to the large α_{95} of the specimen-mean direction of a site, the critical angles for evaluating whether two average directions are identical at the 95% confidence level are as large as ~10–15°, which may not be proper (Table S4). The large α_{95} of the specimen-mean direction of a site may be due to only 3–5 specimens being available. Considering that the angle between the group-mean direction of 15 groups and the site-mean direction of 27 sites is 1.9°, the A_{95} for 15 groups and 27 sites fit well with the corresponding N-dependent confidence intervals, and our proper sampling strategy, we prefer to use the site-mean direction of 27 sites for further discussion.

Table 1
Site-Mean ChRM Directions of the Bima Fm Volcanic Rocks From the Xigaze Area in the South Central Lhasa Terrane

ID	N	Dg (°)	Ig (°)	Ds (°)	Is (°)	k	α_{95} (°)	Strike (°)	Dip (°)	Plon (°)	Plat (°)
BM17	3	350.9	40.4	353.4	−16.8	154.8	11.7	273	58	51.5	279.1
BM21	4	318.5	14.9	318.4	−18.9	116.1	8.6	234	34	34	320.7
BM22	6	317.3	8.9	316.7	−24.9	50.1	9.6	234	34	30.4	319.4
BM23	9	314.3	10.4	313.6	−23.1	144.2	4.3	234	34	29	322.7
BM24 + 25	5	337.6	7.9	338.9	−25.1	60.9	9.9	234	34	42.8	297.1
BM36 + 37	7	322.6	3.3	322.4	−30.7	21.2	13.4	234	34	31.5	311.9
BM38	4	315.1	3.3	313.7	−30.3	72.6	10.9	234	34	26.1	319.2
BM39	7	315	2.7	313.5	−30.8	20.2	13.8	234	34	25.8	319.1
BM40	5	316.5	7.6	315.6	−28.1	49.1	11	234	36	28.3	318.8
BM41	4	321.4	3.7	321	−32.2	52.3	12.8	234	36	29.9	312.4
BM42	3	320.4	1.5	319.6	−34.4	77.9	14.1	234	36	27.9	312.6
BM45	5	323.4	−2.9	323.3	−38.9	108.2	7.4	234	36	27.7	307.3
BM47	3	324.5	7.9	324.6	−28.1	71.5	14.7	234	36	34	311.1
BM55	4	323.1	27	322.8	−29.7	157.1	7.4	246	58	32.2	312
XT16	4	313	−1.7	308.8	−40.5	67	11.3	236	40	18	317.5
XT18	6	324.5	7.6	324.3	−32.4	757.5	2.4	236	40	31.7	309.4
XT19	7	304	8.1	300.9	−20	87.2	6.5	259	40	20.6	333
XT20	6	159.9	1.9	156.9	41.3	60.3	8.7	259	40	−32.4	113.8
XT21	8	322.7	6.8	318.8	−28.7	330.9	3	259	40	30.2	315.9
Mean of section A	19	321.9	8.2	321.4	−29.7	43.3	5.2			31.2	313.1
										K = 46.2	A_{95} = 5.0
BM26	6	295.8	25.0	295.0	−30.4	26.6	13.2	220	57	12.4	331.6
BM27	3	318.7	22.8	319.8	−31.9	81.9	13.7	216	56	29.3	313.7
BM28	7	187.2	−30.8	174.6	2.4	573.8	3.1	216	56	−59	99.2
BM29	6	146.4	−27.3	139.8	11.2	52.6	9.3	184	56	−37.9	143.2
BM30	5	328	0.6	341.3	−28.8	52	12.2	184	56	41.7	293.2
BM32	4	320.8	22.9	320.9	−23.5	59.6	13.9	200	53	33.8	316.6
BM33	4	334.5	7.1	338.2	−14.0	55.1	13.2	176	58	47.9	302
BM34	3	323.2	2.5	336	−23.2	70.6	14.8	170	66	42.5	301.3
Mean of section B	8	326.4	18.2	328.8	−21.6	17.0	13.8			39.1	310.1
										K = 19.0	A_{95} = 13.0
Mean	27	323.2	11.1	323.7	−27.4	28.3	5.3			33.5	312.3
										K = 31.9	A_{95} = 5.0

Note. ID: site label; n: samples used to calculate mean; Dg, Ig and Ds, Is: declination and inclination in geographic and stratigraphic coordinates, respectively; *k*: the best estimate of the precision parameter; α_{95}: 95% confidence cone (Fisher statistics) after tilt correction; K and A_{95} same for virtual geomagnetic poles; Plat and Plon: latitude and longitude of paleopoles in stratigraphic coordinates. The fold test for the final 27 site-mean ChRM directions is positive: The McFadden (1990) fold test is positive at 95% and 99% confidence levels. “Xi” test: critical Xi at 95% = 6.04 and 99% = 8.55, respectively. “Xi1” and “Xi2” IS = 6.68 and 8.58, “Xi1” and “Xi2” TC = 5.42 and 1.26, respectively. The McFadden & McElhinny (1990) reversals test is positive at 95% confidence level, at classification C, when calculating the specimen-mean direction of site BM29 as a normal polarity. Normal polarity: N_1 = 25, D_1 = 321.8°, I_1 = −27.6°, k_1 = 37.3; Reverse polarity: N_2 = 2, D_2 = 167.0°, I_2 = 22.1°, k_2 = 7.5. The McFadden & McElhinny (1990) reversals test is also positive at 95% confidence level, at classification C, when calculating the specimen-mean direction of site BM29 as a reverse polarity. Normal polarity: N_1 = 24, D_1 = 321.9°, I_1 = −28.3°, k_1 = 38.3; Reverse polarity: N_2 = 3, D_2 = 157.2°, I_2 = 18.7°, k_2 = 9.5.

10.1029/2022JB025577

4. Discussion

4.1. The Location of the Lhasa Terrane at ∼180 Ma

With an increasing number of paleomagnetic data sets becoming available, we suggest that a reliable paleomagnetic result should meet the following criteria: (a) structural control; (b) well-determined rock age; (c) stepwise demagnetizations; (d) containing at least 25 paleomagnetic specimens (or eight independent sites); (e) providing a robust field test or reversal test (Meert et al., 2020; Van der Voo, 1990).

The Sangri Group volcanic rocks from the southern margin of the Lhasa terrane have been dated at various ages ranging from Middle Triassic to Early Cretaceous (Hu et al., 2014; C. Wang et al., 2016). Previous paleomagnetic results of the Sangri Group reported by Li et al. (2016) come from many different outcrops in the eastern part of the Lhasa terrane. Because previous paleomagnetic results near Sangye town have no precise ages, we only used their Sangri Group results from the Sangri area with an age of ∼180 Ma in the following discussion (Li et al., 2016) (Table S5). We note here that only two Early Jurassic paleomagnetic data sets meet the above-mentioned criteria, one from the Xigaze area (this study) and one from the Sangri area (Li et al., 2016). A reference location (29.3°N, 90.3°E) on the Yarlung Zangbo suture zone with longitude in between that of the two sampling areas (88.6°E and 92.0°E) was chosen to recalculate the paleolatitude for the Lhasa terrane in the Early Jurassic (Table S6). In addition, reliable paleolatitudes of the Lhasa terrane, North Qiangtang terrane, and Tethyan Himalaya terrane are shown in Figures 9a and 9b (data are tabulated in Table S7).

The observed paleolatitudes for the Lhasa terrane from the Bima Formation are 16 ± 5°S at ∼173–183 Ma (this study) and 0 ± 5°S at ∼180 ± 7 Ma (Li et al., 2016), respectively, yielding a paleolatitude difference of 16 ± 7° (Table S7). Because the distance between two separate sampling areas is only approximately 400 km, the paleolatitudinal distinction cannot be explained only by the longitude difference between the two sampling areas (e.g., Ma, Wang, et al., 2022; Yi et al., 2015). The difference may be due to the Lhasa terrane's northward motion during the Early Jurassic or an insufficient averaging of paleosecular variation. The first interpretation is supported by the stratigraphic level distribution of the sampling sites in the Bima formation, which shows that the exact age of the sampling unit in the Sangri area should be younger than ∼180 Ma, that is, the age of the sampling unit of Section A of this study (Figure 2b). These observations are consistent with the northward movement of the Lhasa terrane during the Jurassic (e.g., Li et al., 2016; Zhou et al., 2016).

The southernmost site from the Sangri section, near the stratigraphic unit dated at ∼180 Ma by Li et al. (2016), has an inclination value (∼35.5°) similar to that of the mean inclination of Section A (∼29.7°), which supports the consistency of our results with those of Li et al. (2016) (Figure 2c; see details in the Supporting Information of Li et al. [2016]). Combining paleomagnetic data from different stratigraphic levels can average the paleosecular variation, increasing the reliability of paleomagnetic results (Otofuji et al., 2007). Although the age of the topmost Sangri section of Li et al. (2016) is unknown, the age of the sampling unit from the Sangri section and that of this study overlap at ∼180 Ma. In addition, the equal-area projections of the ChRM directions or VGPs of 57 sites from this study and the Sangri section of Li et al. (2016) are intersectional (Figures 8c and 8d). Therefore, to better average the paleosecular variation, we combine them to calculate a reliable paleopole at ∼180 Ma (Table S6). A Fisherian average of the 57 sites VGPs yields a paleopole at 44.6°N, 310.1°E, with K = 21.3 and A_{95} = 4.2°, with a corresponding paleolatitude of 8 ± 4°S for the reference location (Table S6). The A_{95} value of the new paleopole falls within the *N*-dependent confidence interval (2.4°, 6.4°) and thus can be fully explained by paleosecular variation (Deenen et al., 2011).

The declination is susceptible to local vertical axis rotation, which may influence the Fisher mean direction and the paleolatitude calculation. Notably, the calculation of inclination-only mean (corresponding to paleolatitude-only) following the method of Arason and Levi (2010) can exclude the influence of local vertical axis rotation. An inclination-only mean for the reference point (29.3°N, 90.3°E) is −14.5 ± 6.3°, based on the Arason and Levi (2010) method, corresponding to a paleolatitude at 7 ± 3°S (Table S6). Two different calculation methods delivered essentially identical paleolatitudes, implying that the influence of declination difference observed between Xigaze and Sangri can be neglected. Therefore, we use the paleolatitude of 8 ± 4°S at ∼180 Ma for the reference location of the Lhasa terrane in the discussion below.

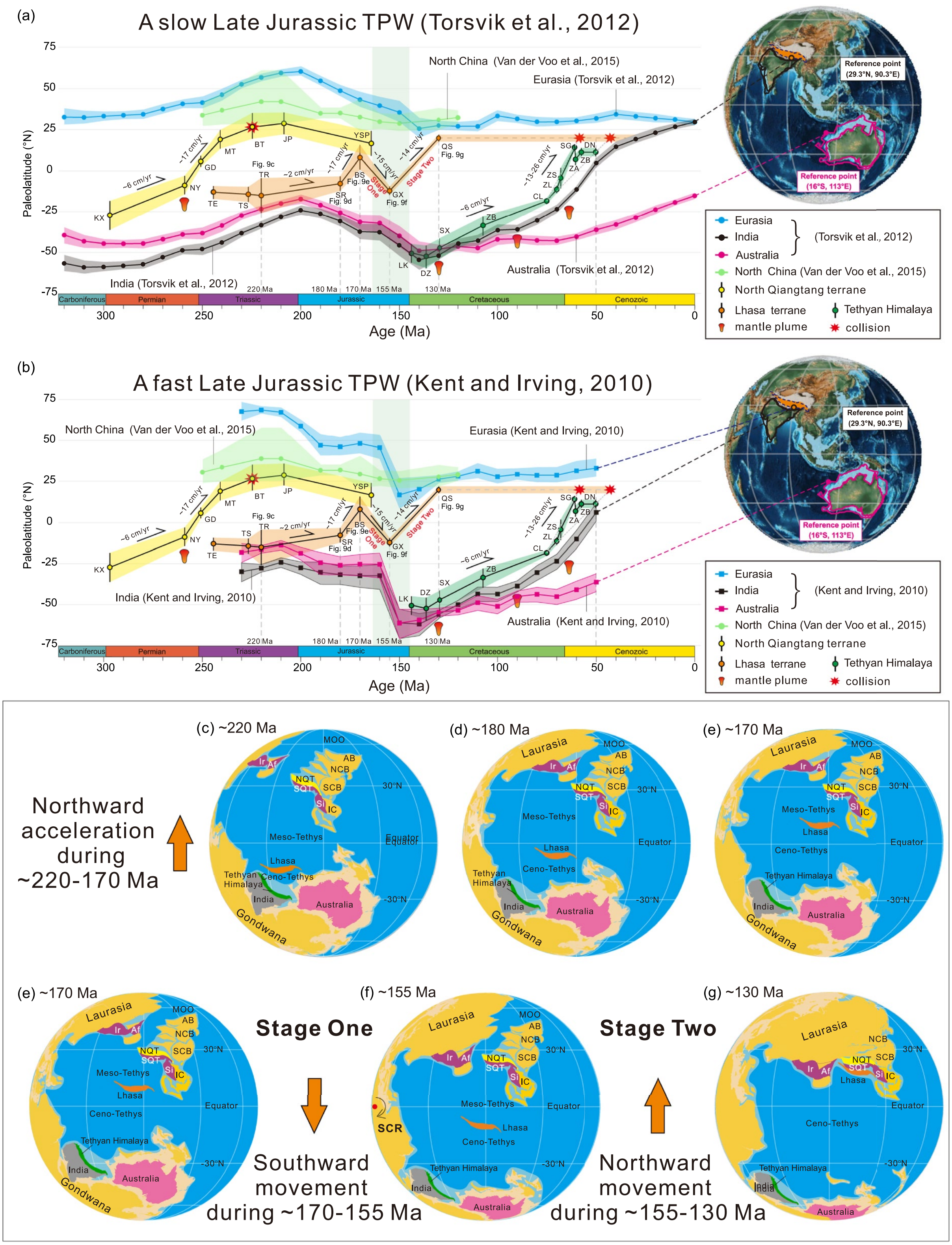
(a)
A slow Late Jurassic TPW (Torsvik et al., 2012)
North China (Van der Voo et al., 2015)
Eurasia (Torsvik et al., 2012)
India (Torsvik et al., 2012)
Australia (Torsvik et al., 2012)
Paleolatitude (°N)
Age (Ma)
Reference point (29.3°N, 90.3°E)
Reference point (16°S, 113°E)
Eurasia
India
Australia
(Torsvik et al., 2012)
North China (Van der Voo et al., 2015)
North Qiangtang terrane
Lhasa terrane
Tethyan Himalaya
mantle plume
collision
Carboniferous
Permian
Triassic
Jurassic
Cretaceous
Cenozoic
(b)
A fast Late Jurassic TPW (Kent and Irving, 2010)
North China (Van der Voo et al., 2015)
Eurasia (Kent and Irving, 2010)
India (Kent and Irving, 2010)
Australia (Kent and Irving, 2010)
(Kent and Irving, 2010)
(c) ~220 Ma
(d) ~180 Ma
(e) ~170 Ma
Northward acceleration during ~220-170 Ma
(e) ~170 Ma
(f) ~155 Ma
(g) ~130 Ma
Stage One
Southward movement during ~170-155 Ma
Stage Two
Northward movement during ~155-130 Ma
Laurasia
Meso-Tethys
Ceno-Tethys
Lhasa
Tethyan Himalaya
India
Australia
Gondwana
Equator
30°N
-30°N
SCR

Figure 9.

4.2. Lhasa Terrane's Acceleration in the Jurassic: Implication for Tethys Evolution

Previous studies from orogens have shown that the declination from a single location is indeed less suited to constrain the rotation of a terrane due to potential variability of local vertical axis rotation, while the inclination is immune to vertical axis rotations and thus can be used to calculate the paleolatitude of a terrane (e.g., Chen et al., 2012; Ma et al., 2014). Paleolatitude observations of the Jurassic show that the Lhasa terrane and India-Australia moved northward and southward, respectively, indicating that the Lhasa terrane separated from India-Australia no later than the Early Jurassic (Figures 9a and 9b) (Li et al., 2016). The divergence of the Lhasa terrane and India-Australia during the Jurassic reveals a continuous extension of the Ceno-Tethys seafloor until it reaches its maximum width at the Jurassic-Cretaceous boundary (Ma et al., 2018).

Li et al. (2016) suggest that the Lhasa terrane moved northward at an average rate of ~5 cm/yr from ~220 to ~130 Ma under the premise of pure N-S motion and no rotation of the Lhasa terrane. With more paleomagnetic results of this time interval becoming available, a reappraisal may unlock more detail. Our updated paleomagnetic results from the Lhasa terrane reveal that it was located at 8 ± 4°S for our reference location (29.3°N, 90.3°E) at ~180 Ma (Figures 9a and 9b). In addition, Otofuji et al. (2007) reported paleomagnetic results from Middle Jurassic red sandstones of the Sangba Formation in the Basu area of the Lhasa terrane. The sedimentary origin fabric with a low degree (Pj) of anisotropy indicates no significant tectonic deformational effects. Positive fold and reversal tests suggest that the characteristic paleomagnetic directions are primary. The characteristic paleomagnetic directions of eight sites yield a paleopole located at 66.8°N, 294.1°E, with A_{95} = 7.4° falling within the N-dependent confidence interval (5.2°, 22.1°) (Deenen et al., 2011), corresponding to a paleolatitude of 8 ± 7°N at ~170 Ma. This result meets our data quality criteria and thus is considered a reliable paleomagnetic result (Table S7). Therefore, the reference location moved from 15 ± 11°S in the Late Triassic (~201–237 Ma), as suggested by paleomagnetic observations from the Coqen area (30.9°N, 84.7°E) (Zhou et al., 2016), to 8 ± 4°S at ~180 Ma (this study) and then to 8 ± 7°N at ~170 Ma (Otofuji et al., 2007), revealing that the northward velocity of the Lhasa terrane changed from ~2 ± 3 cm/yr during ~220-180 Ma to ~17 ± 9 cm/yr during ~180-170 Ma (Figures 9a–9e; Table S7).

Notably, three available Cretaceous paleomagnetic investigations from the intercalated basalt flows and redbeds reveal consistent inclinations, indicating that no significant inclination shallowing has occurred in these redbeds (Cao et al., 2017; Li et al., 2013; Sun et al., 2006), the possible inclination shallowing is still a critical and unresolved problem for paleomagnetic data from redbeds (e.g., Bian et al., 2020; Ding et al., 2015; van Hinsbergen et al., 2012; Sun et al., 2012; Yang, Ma, Zhang, et al., 2015). Even if the red sandstones reported by Otofuji et al. (2007) would have suffered from inclination shallowing with a flattening factor of f = 0.6, the corrected paleolatitude would change from ~8°N to ~13°N, which still falls within the confidence interval of (1°N, 15°N) for the uncorrected paleolatitude of ~8°N. Furthermore, such an inclination shallowing correction would yield an even higher northward velocity of ~23 cm/yr for ~180–170 Ma than the ~17 cm/yr uncorrected number. So, the significant acceleration of the Lhasa terrane during the Jurassic is not an artifact of inclination shallowing. But the higher plate movement velocity is not likely, especially for the time interval when a potential southward TPW occurred (Torsvik et al., 2012). Therefore, we prefer the uncorrected result in the following discussion.

Plate acceleration within the Tethys realm is also traced in the northward journeys of the North Qiangtang terrane, India Craton, and Tethyan Himalaya terrane. High-quality paleomagnetic results in the North Qiangtang terrane reveal that it drifted northward from 28 ± 9°S at ~297 Ma (Song et al., 2017), to 8 ± 6°S at ~259 Ma (Ma et al., 2019), to 6 ± 3°N at ~251 Ma (Guan et al., 2021), to 19 ± 6°N at ~241 Ma (Song et al., 2020), to 26 ± 8°N at ~225 Ma (Yu et al., 2022), and to 29 ± 7°N at ~209 Ma (Song et al., 2015), revealing a significant acceleration

Figure 9. (a and b) Paleolatitude evolution of the Lhasa terrane and adjacent blocks generated using www.paleomagnetism.org (Koymans et al., 2016). The observed paleolatitudes of Lhasa, North Qiangtang and the Tethyan Himalaya are calculated from Table S7. Eurasian, Gondwana-India, and Gondwana-Australia paleolatitudes are from Torsvik et al. (2012) and Kent & Irving (2010), showing a slow TPW (a) and a fast TPW (b) in the Late Jurassic, respectively; those of North China are from Van der Voo et al. (2015). The paleolatitudes of Australia are calculated at a reference location (16°S, 113°E), and other paleolatitudes are calculated at a reference location (29.3°N, 90.3°E). We choose these two reference locations just because Australia is now too far away from the Lhasa terrane, and do not imply that these two reference points were initially next to each other. Significant accelerations of the Lhasa terrane, North Qiangtang terrane, India Craton and Tethyan Himalaya during their northward journey are revealed based on their paleolatitude evolution (See Section 4.2 for more detail). (c–g) The corresponding paleogeography of the Lhasa terrane and adjacent blocks in the Tethyan realm at ~220 Ma, ~180 Ma, ~170 Ma, ~155 Ma and ~130 Ma. The reconstruction uses Gplates based on paleolatitude evolution in Figure 9b. The paleolatitude of the Lhasa terrane at 180 Ma is recalculated with our updated dataset from Li et al. (2016) and this study (Table S6). SCR in Figure 9f means significant clockwise rotation. Other Abbreviations: AB = Amuria Block; Af = Afghanistan; IC = Indochina; Ir = Iran; MOO = Mongol-Okhotsk Ocean; NCB = North China Block; NQT = North Qiangtang terrane; SCB = South China Block; Si = Sibumasu; SQT = South Qiangtang terrane.

from ~6 cm/yr during ~297-259 Ma to ~17 cm/yr during ~259-241 Ma (Figures 9a and 9b; Table S7). India kept moving northward since it separated from Gondwana at ~130 Ma (Bian et al., 2019; van Hinsbergen et al., 2011). The paleolatitude evolution of India shows that it accelerates during the Cretaceous, especially at 90 and 65 Ma, respectively (Figures 9a and 9b) (Bian et al., 2021, 2022; Cande & Stegman, 2011; van Hinsbergen et al., 2011; Meng et al., 2020; Patzelt et al., 1996; Qin et al., 2019; Torsvik et al., 2012; Yi et al., 2011; Yuan et al., 2021). The Tethyan Himalaya moved northward from ~47°S at ~130 Ma (Ma et al., 2016), to ~19°S at ~75 Ma (Yuan et al., 2021), and to ~11–14°N at ~61-50 Ma (e.g., Bian et al., 2021; Yuan et al., 2021, 2022), revealing a significant acceleration from ~6 cm/yr during ~130-75 Ma to ~13 cm/yr during ~75-50 Ma or even up to ~26 cm/yr during ~75-61 Ma, leading to a possible separation of the Tethyan Himalaya terrane from India (Figures 9a and 9b; Table S7) (e.g., Ma et al., 2016; van Hinsbergen et al., 2012; Yang, Ma, Bian, et al., 2015; Yuan et al., 2021). Because the northward journey of the South Qiangtang terrane from Gondwana to Asia occurred prior to the Jurassic (Song et al., 2012, 2015) and reliable paleomagnetic results from the South Qiangtang terrane are nearly restricted to Late Triassic or younger (e.g., Cao et al., 2019, 2020; Chen et al., 2017; Meng et al., 2018; Song et al., 2012), its velocity change during the northward movement in the Permian-Triassic is not really constrainable with robust paleomagnetic results.

Previous studies have shown that slab-pull forces caused by oceanic slab subduction are critical drivers of plate motion (Chen et al., 2020; Conrad & Lithgow-Bertelloni, 2002). The acceleration of individual plates is generally ascribed to mantle plumes and subduction tectonics (Chen et al., 2020; van Hinsbergen et al., 2011). Because no mantle plume activity is known in the Lhasa terrane at ~180-145 Ma, the slab pull force is considered the dominant driving force for accelerating the Lhasa terrane. The initial subduction of the oceanic crust of the Bangong-Nujiang Ocean (Meso-Tethys) in the Early Jurassic (Li et al., 2019) is consistent with the acceleration of the Lhasa terrane during this period.

Previous paleomagnetic, paleontological, and magmatic constraints indicated that the North Qiangtang terrane moved northward together with the South China Block until the Late Permian (Huang et al., 1992; Ma et al., 2019; J. Wang et al., 2018; Y. C. Zhang et al., 2013) when the Emeishan plume triggered their breakup (e.g., Chung et al., 1998). The velocity increase of the North Qiangtang terrane can also be explained by an increased slab pull and ridge push efficiency resulting from the decoupling of microcontinental lithosphere-asthenosphere due to the Emeishan plume activity at ~260 Ma. This effect, suggested by Kumar et al. (2007), has been used to explain the acceleration of the India-Asia convergence (van Hinsbergen et al., 2011).

The acceleration of India was attributed to mantle plume activity (Cande & Stegman, 2011; Yuan et al., 2021, 2022) or (double northward) subduction of the Ceno-Tethys oceanic crust (Jagoutz et al., 2015). Notably, numerical models by van Hinsbergen et al. (2011) suggest that a mantle plume can only lead to an absolute Indian plate motion acceleration of several cm/yr. Therefore, slab-pull forces are most plausible to explain India's northward movement and accelerations in the Cretaceous. It has been documented that India rotated anticlockwise during its northward movement (Huang, van Hinsbergen, Lippert, et al., 2015; Patriat & Achache, 1984; Torsvik et al., 2012). Its rotation allows slab-pull forces to be increasingly transmitted to the passive continental margin, leading to the northward acceleration of the India Craton. In addition, the potential extension between the Tethyan Himalaya and India can also be explained by enhanced slab pull forces related to the subduction of the Ceno-Tethyan mid-oceanic ridge at ~105 Ma (Sun, Lin, et al., 2018; Zahirovic et al., 2016; C. Zhang et al., 2019) or slab rollback at ~80–100 Ma (Ma et al., 2013). The ocean-ridge subduction indicates that the ridge push has disappeared. In this case, slab-pull forces due to subduction could be transmitted to the lithosphere on the opposite side. Therefore, after the ocean-ridge subduction, enhanced slab-pull forces related to ocean-ridge subduction and slab rollback may lead to plate acceleration (Dan, Wang, Murphy, et al., 2021; Dan, Wang, White, et al., 2021; Gutierrez-Alonso et al., 2008; Murphy et al., 2006; Sun, Liu, et al., 2018).

4.3. Further Implications for the Late Jurassic True Polar Wander

The motion of continents relative to the geodynamo reflects the combined effect of the drift of individual continents relative to the mantle and a rotation of both lithosphere and mantle relative to its spin axis, that is, the TPW (Evans, 2003; Torsvik et al., 2012). Paleomagnetism used to reconstruct the motion of continents and oceans have shown the existence of a Jurassic TPW event (e.g., Fu & Kent, 2018; Kent & Irving, 2010; Muttoni & Kent, 2019; Torsvik et al., 2012). Two models have been proposed based on paleomagnetic data filtered by different methods. Based on extensive paleomagnetic data sets with a quality factor Q ≥ 3 (Van der Voo, 1990) from volcanic and

10.1029/2022JB025577

sedimentary poles after correction for inclination shallowing, Torsvik et al. (2012) suggested an ~30.5° TPW event that lasted for the entire Jurassic (200-140 Ma) with a clockwise rotation about an Euler pole at 0°N, 11°E by a velocity of ~0.45–0.8°/Myr. Kent & Irving (2010) used paleomagnetic poles from primarily igneous rocks and sedimentary results after inclination correction to construct the Jurassic TPW during 160-145 Ma. A similar rotation amplitude from ~160 to ~145 Ma reveals a rotation velocity of ~2°/Myr for the Late Jurassic TPW event. Even though two different Jurassic TPW models suggest a similar total rotational amplitude, there is a major dispute about whether there was a "monster shift" TPW in the Late Jurassic. The monster shift in the Late Jurassic may be averaged out within a limited time interval due to the emphasis on paleomagnetic data from sedimentary rocks (Gao et al., 2021), or obscured by the inclusion of numerous problematical poles in the Torsvik et al. (2012)'s model (Kent et al., 2015).

Although the Jurassic TPW is proposed based on paleomagnetic poles from the Pangea continent and not from East Asia, which includes the North China Block (Gao et al., 2021), the two models of Jurassic TPW should lead to southward displacement for East Asia. This conclusion has been proven by recent paleomagnetic results from the North China Block, showing southward motion after ~170 Ma, even though the scale of southward displacement is not in agreement (Gao et al., 2021; Yi et al., 2019). Similarly, the Lhasa terrane, located ~80° to the east of the Euler rotation pole of the TPW during its northward journey in the Jurassic, must also be influenced by the south-directed TPW (Figure 9f). This influence is because it was approximately orthogonal to the rotation axis of the Jurassic TPW (Gao et al., 2021; Li et al., 2022) and at near-equatorial latitudes at ~180-155 Ma (Li et al., 2016, 2022), the primary influence of TPW during this period was latitudinal displacement (Figure 9f). Therefore, the Lhasa terrane is an ideal natural laboratory for evaluating the possible effects of short-lived TPW (Li et al., 2022). Li et al. (2022) suggested that the similar paleolatitudes of the Lhasa terrane at ~180 Ma and ~155 Ma reflect the interplay between its northward plate tectonic motion and the simultaneous TPW, which masked its northward motion in the light of absolute paleolatitude. However, Li et al. (2022) could not really constrain the duration of the recently debated short-lived latest Jurassic-earliest Cretaceous TPW.

Based on our updated paleolatitude evolution of the Lhasa terrane (Figures 9a and 9b), available paleomagnetic results of ~180 Ma and ~170 Ma have shown a significant northward motion of the Lhasa terrane from 8°S to 8°N. Similarly, paleomagnetic results of ~170 Ma rocks (Otofuji et al., 2007) and ~130 Ma rocks, as observed in the Yanhu area (32.3°N, 82.6°E) (Ma et al., 2014), also show a significant northward motion of the Lhasa terrane from 8°N to 20°N. In addition, new paleomagnetic results with positive fold and reversal tests reported by Li et al. (2022) position the Lhasa terrane at a paleolatitude of 12 ± 3°S at 155 ± 2 Ma. Thus, the overall northward motion during ~170-130 Ma should be subdivided into two stages, including a southward drift during ~170-155 Ma and a subsequent northward drift during ~155-130 Ma (Figures 9e–9g, Table S7).

Li et al. (2022) suggested that the Jurassic TPW translated the Lhasa terrane to a more southerly latitude during ~180-155 Ma. Our updated paleolatitude evolution further constrains the southward translation into the time interval from ~170 Ma (Middle Jurassic) to ~155 Ma. As we have shown in Section 4.2 regarding absolute paleolatitude, the northward acceleration during ~180-170 Ma can be explained well by subduction tectonics. Because the effect of the Jurassic TPW during this period is a southward translation (Li et al., 2022; Torsvik et al., 2012), we suggest that the influence of the TPW during ~180-170 Ma is insignificant, if any (Gao et al., 2021; Torsvik et al., 2012). In contrast, the southward drift during ~170-155 Ma can only be explained by a fast south-directed TPW before ~155 Ma (Figure 9f). However, our updated paleolatitude evolution can neither confirm nor reject the long-lived TPW episode that lasts for the entire Jurassic.

Given that the age of the red sandstones reported by Otofuji et al. (2007) is assigned to the Middle Jurassic, the south-directed TPW before ~155 Ma most likely took place during the Late Jurassic, leading to a significant southward shift from ~8°N at ~170 Ma (Otofuji et al., 2007) to ~12°S at ~155 Ma (Li et al., 2022). The southward shift of ~20° occurred in ~15 Myr (~170-155 Ma), which could be attributed to the interplay between the northward motion of the Lhasa terrane and the potential "monster shift" TPW (Gao et al., 2021; Kent et al., 2015; Kent & Irving, 2010; Yi et al., 2019). Considering the northward motion of ~17 cm/yr during ~180-170 Ma, the potential "monster shift" TPW should lead to a southward displacement of the Lhasa terrane larger than ~20° during ~170-155 Ma.

Reliable paleomagnetic results with positive fold and/or reversal tests indicate that the Qiangtang terrane was located at a paleolatitude of ~17 ± 7°N at ~171-158 Ma (Yan et al., 2016) (Figures 9a and 9b; Table S7). This paleolatitude, together with its paleolatitude of ~29°N in the Late Triassic (Song et al., 2015), reveals a southward movement during the Jurassic, which is consistent with the movement of Eurasia and North China Block (Torsvik et al., 2012; Van der Voo et al., 2015) (Figures 9a and 9b). Because the Lhasa-Qiangtang collision occurred after 155 Ma (Kapp et al., 2007; Ma et al., 2018; Zhu et al., 2016) and the Lhasa terrane was located at ~8°N at ~170 Ma (Figures 9a and 9b; Table S7), the convergence between the Lhasa and Qiangtang terranes during ~170-155 Ma should be less than ~9° to avoid a collision prior to ~155 Ma. Therefore, the amplitude of the TPW during ~170-155 Ma would be ~20–29°. The Middle Jurassic paleomagnetic results do not come with an exact age and their A_{95} of 7.4° is rather large (Figures 9a and 9b). Therefore, caution should be taken when interpreting the calculated value of the TPW. Nevertheless, our updated constraint on the Jurassic TPW, which fits well with that observed from the North China Block (Gao et al., 2021; Yi et al., 2019), supports the existence of a fast Late Jurassic TPW.

TPW implies that all continents underwent a consistent rotation about an Euler pole. Figures 9a and 9b show the paleolatitude evolution of the Lhasa terrane and its adjacent blocks. The minor difference in the paleolatitude evolution of Eurasia and India-Australia in the Late Jurassic may be due to the opening of the Central Atlantic Ocean in the Jurassic (Labails et al., 2010). The paleolatitude approach of Eurasia and the North China Block reflects the closure of the Mongol-Okhotsk Ocean between Siberia and the eastern Asian blocks (Figure 9) (Torsvik et al., 2012; Van der Voo et al., 2015). Notably, even though their magnitude may differ, the expected paleolatitude evolution of Eurasia, India, Australia, and the North China Block reveal southward motion during the Late Jurassic, which is consistent with the TPW in this period. A fast Late Jurassic TPW implied by our updated paleolatitude evolution of the Lhasa terrane is also supported by the significant southward movement calculated by Kent and Irving (2010) (Figure 9b). The minor difference in the Late Jurassic between the observed southward motion of the Lhasa terrane and the expected southward motion of Eurasia, India, and Australia may be due to the Lhasa-Eurasia convergence and the large confidence limit of age and paleolatitudes for the Lhasa terrane in the Middle Jurassic.

The subsequent northward drift with an average velocity of ~14 cm/yr during ~155-130 Ma also fits well with the combined effect of northward movement of the Lhasa terrane and northward TPW after ~155 Ma (Li et al., 2022). Therefore, the yoyo-like movement of the Lhasa terrane near the equator before and after ~155 Ma supports a fast Late Jurassic TPW event on a ~10 Myr timescale.

5. Conclusions

We report new paleomagnetic results from 27 sites in the volcano-sedimentary sequence of the Bima Formation dated at ~173–180 Ma. Our results fulfill all seven paleomagnetic quality criteria updated by Meert et al. (2020). These results, together with previous Triassic-Cretaceous paleomagnetic results from the Lhasa terrane, reveal that it was located at 8 ± 4°S at ~180 Ma for the reference point (29.3°N, 90.3°E) and that its northward motion accelerated from ~2 cm/yr during ~220-180 Ma to ~17 cm/yr during ~180-170 Ma. A review of high-quality paleolatitude data suggests significant accelerations of the North Qiangtang terrane, India Craton and Tethyan Himalaya during their northward journeys from Gondwana to Asia. The significant accelerations related to the slab pull forces due to slab subduction (Wan et al., 2019) may be a common feature of these Gondwana-derived microcontinents. The updated paleolatitude evolution, from ~8°N at ~170 Ma to ~12°S at ~155 Ma and then to 20°N at ~130 Ma, reveals an oscillatory motion of the Lhasa terrane, providing strong evidence for the occurrence of the fast Late Jurassic TPW, which has not yet been confirmed or rejected by Li et al. (2022).

Conflict of Interest

The authors declare no conflicts of interest relevant to this study.

Data Availability Statement

Our data in this study are available in the Supporting Information, and also available for download through Figshare at 10.6084/m9.figshare.19387688.

Acknowledgments

We are grateful to four anonymous reviewers and associate editor Adrian Muxworthy for their constructive comments. We also thank Yongtao Li, Haiyan Li, Yingchao Xu, Zongmin Zhu, Qiang Liu, and Haijun Xu for providing laboratory instruments and Weimin Ruan, Chao Niu, Chang Xu and Peng Han for their help in the laboratory. This work is supported by the Second Tibetan Plateau Scientific Expedition and Research (STEP) (2019QZKK0702), the National Natural Science Foundation of China (41802242, 42174089, 91855215, 42021002, 41874079, and 42030205), and the Strategic Priority Research Program of Chinese Academy of Sciences (XDA2007030402, XDA17010403, and XDB41010304).

References

An, W., Hu, X. M., Garzanti, E., Wang, J. G., & Liu, Q. (2021). New precise dating of the India-Asia collision in the Tibetan Himalaya at 61 Ma. *Geophysical Research Letters*, *48*(3), e2020GL090641. https://doi.org/10.1029/2020gl090641

Arason, P., & Levi, S. (2010). Maximum likelihood solution for inclination-only data in paleomagnetism. *Geophysical Journal International*, *182*(2), 753–771. https://doi.org/10.1111/j.1365-246X.2010.04671.x

Bian, W., Yang, T., Ma, Y., Jin, J., Gao, F., Zhang, S., et al. (2017). New Early Cretaceous palaeomagnetic and geochronological results from the far Western Lhasa terrane: Contributions to the Lhasa-Qiangtang collision. *Scientific Reports*, *7*(1), 16216. https://doi.org/10.1038/s41598-017-16482-3

Bian, W., Yang, T., Wang, S., Peng, W., Zhang, S., Wu, H., et al. (2022). Cretaceous paleomagnetic and detrital zircon U-Pb geochronological results from the Tethyan Himalaya: Constraints on the Neo-Tethys evolution. *Global and Planetary Change*, *216*, 103903. https://doi.org/10.1016/j.gloplacha.2022.103903

Bian, W. W., Yang, T. S., Jiang, Z. L., Jin, J. J., Gao, F., Wang, S., et al. (2020). Paleomagnetism of the late Cretaceous red beds from the far Western Lhasa terrane: Inclination discrepancy and tectonic implications. *Tectonics*, *39*(8), e2020TC006280. https://doi.org/10.1029/2020tc006280

Bian, W. W., Yang, T. S., Ma, Y. M., Jin, J. J., Gao, F., Wang, S., et al. (2019). Paleomagnetic and geochronological results from the Zhela and Weimei formations lava flows of the eastern Tethyan Himalaya: New insights into the breakup of eastern Gondwana. *Journal of Geophysical Research: Solid Earth*, *124*(1), 44–64. https://doi.org/10.1029/2018jb016403

Bian, W. W., Yang, T. S., Peng, W. X., Wang, S., Gao, F., Zhang, S. H., et al. (2021). Paleomagnetic constraints on the India-Asia collision and the size of greater India. *Journal of Geophysical Research: Solid Earth*, *126*(6), e2021JB021965. https://doi.org/10.1029/2021jb021965

Cande, S. C., & Stegman, D. R. (2011). Indian and African plate motions driven by the push force of the Reunion plume head. *Nature*, *475*(7354), 47–52. https://doi.org/10.1038/nature10174

Cao, Y., Sun, Z. M., Li, H. B., Pei, J. L., Jiang, W., Xu, W., et al. (2017). New Late Cretaceous paleomagnetic data from volcanic rocks and red beds from the Lhasa terrane and its implications for the paleolatitude of the southern margin of Asia prior to the collision with India. *Gondwana Research*, *41*, 337–351. https://doi.org/10.1016/j.gr.2015.11.006

Cao, Y., Sun, Z. M., Li, H. B., Pei, J. L., Liu, D. L., Zhang, L., et al. (2019). New paleomagnetic results from middle Jurassic limestones of the Qiangtang terrane, Tibet: Constraints on the evolution of the Bangong-Nujiang Ocean. *Tectonics*, *38*(1), 215–232. https://doi.org/10.1029/2017TC004842

Cao, Y., Sun, Z. M., Li, H. B., Ye, X. Z., Pan, J. W., Liu, D. L., et al. (2020). Paleomagnetism and U-Pb geochronology of early Cretaceous volcanic rocks from the Qiangtang block, Tibetan plateau: Implications for the Qiangtang-Lhasa collision. *Tectonophysics*, *789*, 228500. https://doi.org/10.1016/j.tecto.2020.228500

Chen, L., Wang, X., Liang, X. F., Wan, B., & Liu, L. J. (2020). Subduction tectonics vs. Plume tectonics-Discussion on driving forces for plate motion. *Science China Earth Sciences*, *63*(3), 315–328. https://doi.org/10.1007/s11430-019-9538-2

Chen, W. W., Yang, T. S., Zhang, S. H., Yang, Z. Y., Li, H. Y., Wu, H. C., et al. (2012). Paleomagnetic results from the early Cretaceous Zenong group volcanic rocks, Cuoqin, Tibet, and their paleogeographic implications. *Gondwana Research*, *22*(2), 461–469. https://doi.org/10.1016/j.gr.2011.07.019

Chen, W. W., Zhang, S. H., Ding, J. K., Zhang, J. H., Zhao, X. X., Zhu, L. D., et al. (2017). Combined paleomagnetic and geochronological study on Cretaceous strata of the Qiangtang terrane, central Tibet. *Gondwana Research*, *41*, 373–389. https://doi.org/10.1016/j.gr.2015.07.004

Chen, X. L., Richards, J. P., Liang, H. Y., Zou, Y. Q., Zhang, J., Huang, W. T., et al. (2019). Contrasting arc magma fertilities in the Gangdese belt, Southern Tibet: Evidence from geochemical variations of Jurassic volcanic rocks updates. *Lithos*, *324*, 789–802. https://doi.org/10.1016/j.lithos.2018.12.008

Chenet, A.-L., Fluteau, F., Courtillot, V., Gerard, M., & Subbarao, K. V. (2008). Determination of rapid Deccan eruptions across the Cretaceous-Tertiary boundary using paleomagnetic secular variation: Results from a 1200-m-thick section in the Mahabaleshwar escarpment. *Journal of Geophysical Research: Solid Earth*, *113*(B4), B04101. https://doi.org/10.1029/2006jb004635

Chung, S. L., Jahn, B. M., Genyao, W., Lo, C. H., & Bolin, C. (1998). The Emeishan flood basalt in SW China: A mantle plume initiation model and its connection with continental breakup and mass extinction at the Permian-Triassic boundary. In M. F. J. Flower, S. L. Chung, C. H. Lo, & T. Y. Lee (Eds.), *Mantle Dynamics and Plate Interactions in East Asia*. (Vol. *27*, pp. 47–58).

Conrad, C. P., & Lithgow-Bertelloni, C. (2002). How mantle slabs drive plate tectonics. *Science*, *298*(5591), 207–209. https://doi.org/10.1126/science.1074161

Dan, W., Wang, Q., Murphy, J. B., Zhang, X. Z., Xu, Y. G., White, W. M., et al. (2021). Short duration of early Permian Qiangtang-Panjal large igneous province: Implications for origin of the Neo-Tethys ocean. *Earth and Planetary Science Letters*, *568*, 117054. https://doi.org/10.1016/j.epsl.2021.117054

Dan, W., Wang, Q., White, W. M., Li, X.-H., Zhang, X.-Z., Tang, G.-J., et al. (2021). Passive-margin magmatism caused by enhanced slab-pull forces in central Tibet. *Geology*, *49*(2), 130–134. https://doi.org/10.1130/g47957.1

Day, R., Fuller, M., & Schmidt, V. A. (1977). Hysteresis properties of titanomagnetites: Grain-size and compositional dependence. *Physics of the Earth and Planetary Interiors*, *13*(4), 260–267. https://doi.org/10.1016/0031-9201(77)90108-X

Deenen, M. H. L., Langereis, C. G., van Hinsbergen, D. J. J., & Biggin, A. J. (2011). Geomagnetic secular variation and the statistics of palaeomagnetic directions. *Geophysical Journal International*, *186*(2), 509–520. https://doi.org/10.1111/j.1365-246X.2011.05050.x

Dewey, J. F., Shackleton, R. M., Chang, C. F., & Sun, Y. Y. (1988). The tectonic evolution of the Tibetan Plateau. *Philosophical Transactions of the Royal Society A: Mathematical, Physical & Engineering Sciences*, *327*(1594), 379–413. https://doi.org/10.1098/rsta.1988.0135

Ding, J., Zhang, S., Chen, W., Zhang, J., Yang, T., Jiang, G., et al. (2015). Paleomagnetism of the Oligocene Kangtuo formation red beds (Central Tibet): Inclination shallowing and tectonic implications. *Journal of Asian Earth Sciences*, *104*, 55–68. https://doi.org/10.1016/j.jseaes.2014.10.006

Ding, L., Yang, D., Cai, F. L., Pullen, A., Kapp, P., Gehrels, G. E., et al. (2013). Provenance analysis of the Mesozoic Hoh-Xil-Songpan-Ganzi turbidites in northern Tibet: Implications for the tectonic evolution of the eastern Paleo-Tethys ocean. *Tectonics*, *32*(1), 34–48. https://doi.org/10.1002/tect.20013

Dunlop, D. (2002). Theory and application of the Day plot (MRS/Ms versus Hcr/Hc): 1. Theoretical curves and tests using titanomagnetite data. *Journal of Geophysical Research*, *107*(B3), 2056. https://doi.org/10.1029/2001JB000486

Dupont-Nivet, G., Lippert, P. C., van Hinsbergen, D. J. J., Meijers, M. J. M., & Kapp, P. (2010). Palaeolatitude and age of the Indo-Asia collision: Palaeomagnetic constraints. *Geophysical Journal International*, *182*(3), 1189–1198. https://doi.org/10.1111/j.1365-246X.2010.04697.x

Evans, D. A. D. (2003). True polar wander and supercontinents. *Tectonophysics*, *362*(1), 303–320. https://doi.org/10.1016/S0040-1951(02)000642-X

Fu, R. R., & Kent, D. V. (2018). Anomalous Late Jurassic motion of the Pacific Plate with implications for true polar wander. *Earth and Planetary Science Letters*, *490*, 20–30. https://doi.org/10.1016/j.epsl.2018.02.034

Fu, R. R., Kent, D. V., Hemming, S. R., Gutiérrez, P., & Creveling, J. R. (2020). Testing the occurrence of Late Jurassic true polar wander using the La Negra volcanics of northern Chile. *Earth and Planetary Science Letters*, *529*, 115835. https://doi.org/10.1016/j.epsl.2019.115835

Gao, Y., Zhang, S., Zhao, H., Ren, Q., Yang, T., Wu, H., & Li, H. (2021). North China block underwent simultaneous true polar wander and tectonic convergence in late Jurassic: New paleomagnetic constraints. *Earth and Planetary Science Letters*, *567*, 117012. https://doi.org/10.1016/j.epsl.2021.117012

Guan, C., Yan, M., Zhang, W., Zhang, D., Fu, Q., Yu, L., et al. (2021). Paleomagnetic and chronologic data bearing on the Permian/Triassic boundary position of Qamdo in the Eastern Qiantang terrane: Implications for the closure of the Paleo-Tethys. *Geophysical Research Letters*, *48*(6), e2020GL092059. https://doi.org/10.1029/2020gl092059

Gutierrez-Alonso, G., Fernandez-Suarez, J., Weil, A. B., Murphy, J. B., Nance, R. D., Corfu, F., & Johnston, S. T. (2008). Self-subduction of the Pangaean global plate. *Nature Geoscience*, *1*(8), 549–553. https://doi.org/10.1038/ngeo250

Hu, J. R., Fan, Y. C., Nima, C. R., & Chen, G. J. (2014). Regional geological survey report of the People's Republic of China. *Xigaze City (H45C003004), Scale*, *1*, 250000.

Hu, X., Garzanti, E., Wang, J., Huang, W., An, W., & Webb, A. (2016). The timing of India-Asia collision onset—Facts, theories, controversies. *Earth-Science Reviews*, *160*, 264–299. https://doi.org/10.1016/j.earscirev.2016.07.014

Huang, K., Opdyke, N. D., Peng, X., & Li, J. (1992). Paleomagnetic results from the Upper Permian of the eastern Qiangtang terrane of Tibet and their tectonic implications. *Earth and Planetary Science Letters*, *111*(1), 1–10. https://doi.org/10.1016/0012-821X(92)90164-Q

Huang, W., van Hinsbergen, D. J. J., Lippert, P. C., Guo, Z., & Dupont-Nivet, G. (2015). Paleomagnetic tests of tectonic reconstructions of the India-Asia collision zone. *Geophysical Research Letters*, *42*(8), 2642–2649. https://doi.org/10.1002/2015gl063749

Huang, W. T., van Hinsbergen, D. J. J., Maffione, M., Orme, D. A., Dupont-Nivet, G., Guilmette, C., et al. (2015). Lower Cretaceous Xigaze ophiolites formed in the Gangdese forearc: Evidence from paleomagnetism, sediment provenance, and stratigraphy. *Earth and Planetary Science Letters*, *415*, 142–153. https://doi.org/10.1016/j.epsl.2015.01.032

Jagoutz, O., Royden, L., Holt, A. F., & Becker, T. W. (2015). Anomalously fast convergence of India and Eurasia caused by double subduction. *Nature Geoscience*, *8*(6), 475–478. https://doi.org/10.1038/ngeo2418

Kang, Z. Q., Xu, J. F., Wilde, S. A., Feng, Z. H., Chen, J. L., Wang, B. D., et al. (2014). Geochronology and geochemistry of the Sangri group volcanic rocks, southern Lhasa terrane: Implications for the early subduction history of the Neo-Tethys and Gangdese magmatic arc. *Lithos*, *200*, 157–168. https://doi.org/10.1016/j.lithos.2014.04.019

Kapp, P., DeCelles, P. G., Gehrels, G. E., Heizler, M., & Ding, L. (2007). Geological records of the Lhasa-Qiangtang and Indo-Asian collisions in the Nima area of central Tibet. *The Geological Society of America Bulletin*, *119*(7–8), 917–933. https://doi.org/10.1130/B26033.1

Kent, D. V., & Irving, E. (2010). Influence of inclination error in sedimentary rocks on the Triassic and Jurassic apparent pole wander path for North America and implications for Cordilleran tectonics. *Journal of Geophysical Research*, *115*(B10), B10103. https://doi.org/10.1029/2009JB007205

Kent, D. V., Kjarsgaard, B. A., Gee, J. S., Muttoni, G., & Heaman, L. M. (2015). Tracking the Late Jurassic apparent (or true) polar shift in U-Pb-dated kimberlites from cratonic North America (Superior Province of Canada). *Geochemistry, Geophysics, Geosystems*, *16*(4), 983–994. https://doi.org/10.1002/2015gc005734

Kirschvink, J. L. (1980). The least-squares line and plane and the analysis of palaeomagnetic data. *Geophysical Journal International*, *62*(3), 699–718. https://doi.org/10.1111/j.1365-246X.1980.tb02601.x

Koymans, M. R., Langereis, C. G., Pastor-Galan, D., & van Hinsbergen, D. J. J. (2016). Paleomagnetism.org: An online multi-platform open source environment for paleomagnetic data analysis. *Computers & Geosciences*, *93*, 127–137. https://doi.org/10.1016/j.cageo.2016.05.007

Krása, D., Shcherbakov, V. P., Kunzmann, T., & Petersen, N. (2005). Self-reversal of remanent magnetization in basalts due to partially oxidized titanomagnetites. *Geophysical Journal International*, *162*(1), 115–136. https://doi.org/10.1111/j.1365-246X.2005.02656.x

Kumar, P., Yuan, X. H., Kumar, M. R., Kind, R., Li, X. Q., & Chadha, R. K. (2007). The rapid drift of the Indian tectonic plate. *Nature*, *449*(7164), 894–897. https://doi.org/10.1038/nature06214

Labails, C., Olivet, J. L., Aslanian, D., & Roest, W. R. (2010). An alternative early opening scenario for the Central Atlantic Ocean. *Earth and Planetary Science Letters*, *297*(3–4), 355–368. https://doi.org/10.1016/j.epsl.2010.06.024

Lang, X. H., Deng, Y. L., Wang, X. H., Tang, J. X., Yin, Q., Xie, F. W., et al. (2020). Geochronology and geochemistry of volcanic rocks of the Bima Formation, southern Lhasa subterrane, Tibet: Implications for early Neo-Tethyan subduction. *Gondwana Research*, *80*, 335–349. https://doi.org/10.1016/j.gr.2019.11.005

Li, S., Yin, C. Q., Guilmette, C., Ding, L., & Zhang, J. (2019). Birth and demise of the Bangong-Nujiang Tethyan ocean: A review from the Gerze area of central Tibet. *Earth-Science Reviews*, *198*, 102907. https://doi.org/10.1016/j.earscirev.2019.102907

Li, Y. X., Shu, L. S., Wen, B., Yang, Z. Y., & Ali, J. R. (2013). Magnetic inclination shallowing problem and the issue of Eurasia's rigidity: Insights following a palaeomagnetic study of upper Cretaceous basalts and redbeds from SE China. *Geophysical Journal International*, *194*(3), 1374–1389. https://doi.org/10.1093/gji/ggt181

Li, Z., Ding, L., Lippert, P. C., Song, P., Yue, Y., & van Hinsbergen, D. J. J. (2016). Paleomagnetic constraints on the Mesozoic drift of the Lhasa terrane (Tibet) from Gondwana to Eurasia. *Geology*, *44*(9), 727–730. https://doi.org/10.1130/g38030.1

Li, Z., Ding, L., van Hinsbergen, D., Lippert, P., Yahui, Y., Xie, J., et al. (2022). Jurassic true polar wander recorded by the Lhasa terrane on its northward journey from Gondwana to Eurasia. *Earth and Planetary Science Letters*, *592*, 117609. https://doi.org/10.1016/j.epsl.2022.117609

Li, Z. Y., Ding, L., Song, P. P., Fu, J. J., & Yue, Y. H. (2017). Paleomagnetic constraints on the paleolatitude of the Lhasa block during the Early Cretaceous: Implications for the onset of India-Asia collision and latitudinal shortening estimates across Tibet and stable Asia. *Gondwana Research*, *41*, 352–372. https://doi.org/10.1016/j.gr.2015.05.013

Liebke, U., Appel, E., Ding, L., Neumann, U., Antolin, B., & Xu, Q. A. (2010). Position of the Lhasa terrane prior to India-Asia collision derived from palaeomagnetic inclinations of 53 Ma old dykes of the Linzhou basin: Constraints on the age of collision and post-collisional shortening within the Tibetan plateau. *Geophysical Journal International*, *182*(3), 1199–1215. https://doi.org/10.1111/j.1365-246X.2010.04698.x

Liebke, U., Appel, E., Neumann, U., & Ding, L. (2012). Dual polarity directions in basaltic-andesitic dykes-reversal record or self-reversed magnetization? *Geophysical Journal International*, *190*(2), 887–899. https://doi.org/10.1111/j.1365-246X.2012.05543.x

Lippert, P. C., van Hinsbergen, D. J., & Dupont-Nivet, G. (2014). Early Cretaceous to present latitude of the central proto-Tibetan plateau: A paleomagnetic synthesis with implications for Cenozoic tectonics, paleogeography, and climate of Asia. *Geological Society of America Special Papers*, *507*, 1–21.

Lippert, P. C., Zhao, X., Coe, R. S., & Lo, C.-H. (2011). Palaeomagnetism and Ar-40/Ar-39 geochronology of upper Palaeogene volcanic rocks from central Tibet: Implications for the central Asia inclination anomaly, the palaeolatitude of Tibet and post-50 Ma shortening within Asia. *Geophysical Journal International*, *184*(1), 131–161. https://doi.org/10.1111/j.1365-246X.2010.04833.x

Ma, L., Wang, Q., Li, Z. X., Wyman, D. A., Jiang, Z. Q., Yang, J. H., et al. (2013). Early Late Cretaceous (ca. 93 Ma) norites and hornblendites in the Milin area, eastern Gangdese: Lithosphere-asthenosphere interaction during slab rollback and an insight into early Late Cretaceous (ca. 100-80 Ma) magmatic "flare-up" in southern Lhasa (Tibet). *Lithos*, *172*, 17–30. https://doi.org/10.1016/j.lithos.2013.03.007

Ma, Y., Ruan, W., Niu, C., & Yang, T. (2022). Movement history of the microcontinents from the Tibetan plateau based on paleomagnetic results with Sufficient sampling Units. *Journal of Earth Science*, *33*(5), 1072–1080. https://doi.org/10.1007/s12583-022-1721-2

Ma, Y., Wang, Q., Yang, T., Ou, Q., Zhang, X., Dan, W., et al. (2022). Location of the Lhasa terrane in the Late Cretaceous and its implications for crustal deformation. *Palaeogeography, Palaeoclimatology, Palaeoecology*, *588*, 110821. https://doi.org/10.1016/j.palaeo.2021.110821

Ma, Y., Yang, T., Bian, W., Jin, J., Wang, Q., Zhang, S., et al. (2018). A stable southern margin of Asia during the Cretaceous: Paleomagnetic constraints on the Lhasa-Qiangtang collision and the maximum width of the Neo-Tethys. *Tectonics*, *37*(10), 3853–3876. https://doi.org/10.1029/2018tc005143

Ma, Y., Yang, T., Yang, Z., Zhang, S., Wu, H., Li, H., et al. (2014). Paleomagnetism and U-Pb zircon geochronology of Lower Cretaceous lava flows from the Western Lhasa terrane: New constraints on the India-Asia collision process and intracontinental deformation within Asia. *Journal of Geophysical Research: Solid Earth*, *119*(10), 7404–7424. https://doi.org/10.1002/2014jb011362

Ma, Y. M., Wang, Q., Wang, J., Yang, T. S., Tan, X. D., Dan, W., et al. (2019). Paleomagnetic constraints on the origin and drift history of the North Qiangtang terrane in the late Paleozoic. *Geophysical Research Letters*, *46*(2), 689–697. https://doi.org/10.1029/2018gl080964

Ma, Y. M., Yang, T. S., Bian, W. W., Jin, J. J., Wang, Q., Zhang, S. H., et al. (2017). Paleomagnetic and geochronologic results of latest Cretaceous lava flows from the Lhasa terrane and their tectonic implications. *Journal of Geophysical Research: Solid Earth*, *122*(11), 8786–8809. https://doi.org/10.1002/2017jb014743

Ma, Y. M., Yang, T. S., Bian, W. W., Jin, J. J., Zhang, S. H., Wu, H. C., & Li, H. Y. (2016). Early Cretaceous paleomagnetic and geochronologic results from the Tethyan Himalaya: Insights into the Neotethyan paleogeography and the India-Asia collision. *Scientific Reports*, *6*(1), 21605. https://doi.org/10.1038/srep21605

Matthews, K. J., Maloney, K. T., Zahirovic, S., Williams, S. E., Seton, M., & Muller, D. (2016). Global plate boundary evolution and kinematics since the late Paleozoic. *Global and Planetary Change*, *146*, 226–250. https://doi.org/10.1016/j.gloplacha.2016.10.002

McFadden, P. L. (1990). A new fold test for paleomagnetic studies. *Geophysical Journal International*, *103*(1), 163–169. https://doi.org/10.1111/j.1365-246X.1990.tb01761.x

McFadden, P. L., & McElhinny, M. W. (1988). The combined analysis of remagnetization circles and direct observations in paleomagnetism. *Earth and Planetary Science Letters*, *87*(1–2), 161–172. https://doi.org/10.1016/0012-821x(88)90072-6

McFadden, P. L., & McElhinny, M. W. (1990). Classification of the reversal test in paleomagnetism. *Geophysical Journal International*, *103*(3), 725–729. https://doi.org/10.1111/j.1365-246X.1990.tb05683.x

Meert, J. G., Pivarunas, A. F., Evans, D. A. D., Pisarevsky, S. A., Pesonen, L. J., Li, Z. X., et al. (2020). The magnificent seven: A proposal for modest revision of the van der Voo (1990) quality index. *Tectonophysics*, *790*(15), 228549. https://doi.org/10.1016/j.tecto.2020.228549

Meng, J., Gilder, S. A., Li, Y. L., Wang, C. S., & Liu, T. (2020). Expanse of greater India in the late Cretaceous. *Earth and Planetary Science Letters*, *542*, 116330. https://doi.org/10.1016/j.epsl.2020.116330

Meng, J., Wang, C., Zhao, X., Coe, R., Li, Y., & Finn, D. (2012). India-Asia collision was at 24 degrees N and 50 Ma: Palaeomagnetic proof from southernmost Asia. *Scientific Reports*, *2*(1), 925. https://doi.org/10.1038/srep00925

Meng, J., Zhao, X. X., Wang, C. S., Liu, H., Li, Y. L., Han, Z. P., et al. (2018). Palaeomagnetism and detrital zircon U–Pb geochronology of Cretaceous redbeds from central Tibet and tectonic implications. *Geological Journal*, *53*(5), 2315–2333. https://doi.org/10.1002/gj.3070

Metcalfe, I. (2021). Multiple Tethyan ocean basins and orogenic belts in Asia. *Gondwana Research*, *100*, 87–130. https://doi.org/10.1016/j.gr.2021.01.012

Murphy, J. B., Gutierrez-Alonso, G., Nance, R. D., Fernandez-Suarez, J., Keppie, J. D., Quesada, C., et al. (2006). Origin of the Rheic ocean: Rifting along a Neoproterozoic suture? *Geology*, *34*(5), 325–328. https://doi.org/10.1130/g22068.1

Muttoni, G., & Kent, D. V. (2019). Jurassic monster polar shift confirmed by sequential paleopoles from Adria, promontory of Africa. *Journal of Geophysical Research: Solid Earth*, *124*(4), 3288–3306. https://doi.org/10.1029/2018JB017199

Otofuji, Y. I., Mu, C. L., Tanaka, K., Miura, D., Inokuchi, H., Kamei, R., et al. (2007). Spatial gap between Lhasa and Qiangtang blocks inferred from middle Jurassic to Cretaceous paleomagnetic data. *Earth and Planetary Science Letters*, *262*(3–4), 581–593. https://doi.org/10.1016/j.epsl.2007.08.013

Patriat, P., & Achache, J. (1984). India Eurasia collision Chronology has implications for crustal shortening and driving mechanism of plates. *Nature*, *311*(5987), 615–621. https://doi.org/10.1038/311615a0

Patzelt, A., Li, H. M., Wang, J. D., & Appel, E. (1996). Palaeomagnetism of Cretaceous to Tertiary sediments from southern Tibet: Evidence for the extent of the northern margin of India prior to the collision with Eurasia. *Tectonophysics*, *259*(4), 259–284. https://doi.org/10.1016/0040-1951(95)00181-6

Qin, S. X., Li, Y. X., Li, X. H., Xu, B., & Luo, H. (2019). Paleomagnetic results of Cretaceous cherts from Zhongba, southern Tibet: New constraints on the India-Asia collision. *Journal of Asian Earth Sciences*, *173*, 42–53. https://doi.org/10.1016/j.jseaes.2019.01.012

Ran, M. L., Kang, Z. Q., Xu, J. F., Fu, W. C., Yang, F., Wang, B. D., et al. (2017). Geochronology, geochemistry and geological significance of the Bima Formation volcanic rocks located on the southern margin of the Lhasa Block, Xigaze, Tibet. *Geochimica*, *46*(3), 205–218.

Ran, M. L., Kang, Z. Q., Xu, J. F., Yang, F., Jiang, Z. Q., Li, Q., et al. (2019). Evolution of the northward subduction of the Neo-Tethys: Implications of geochemistry of Cretaceous arc volcanics in Qinghai-Tibetan plateau. *Palaeogeography, Palaeoclimatology, Palaeoecology*, *515*, 83–94. https://doi.org/10.1016/j.palaeo.2017.12.043

Roberts, A. P., Almeida, T. P., Church, N. S., Harrison, R. J., Heslop, D., Li, Y. L., et al. (2017). Resolving the origin of pseudo-single domain magnetic behavior. *Journal of Geophysical Research: Solid Earth*, *122*(12), 9534–9558. https://doi.org/10.1002/2017JB014860

Song, C. Y., Wang, J., Fu, X. G., Feng, X. L., Chen, M., & He, L. (2012). Late Triassic paleomagnetic data from the Qiangtang terrane of Tibetan Plateau and their tectonic significances. *Journal of Jilin University (Earth Science Edition)*, *42*, 526–535. (In Chinese with English abstract).

Song, P., Ding, L., Li, Z., Lippert, P. C., Yang, T., Zhao, X., et al. (2015). Late Triassic paleolatitude of the Qiangtang block: Implications for the closure of the Paleo-Tethys ocean. *Earth and Planetary Science Letters*, *424*, 69–83. https://doi.org/10.1016/j.epsl.2015.05.020

Song, P., Ding, L., Li, Z., Lippert, P. C., & Yue, Y. (2017). An early bird from Gondwana: Paleomagnetism of lower Permian lavas from northern Qiangtang (Tibet) and the geography of the Paleo-Tethys. *Earth and Planetary Science Letters*, *475*, 119–133. https://doi.org/10.1016/j.epsl.2017.07.023

Song, P., Ding, L., Lippert, P. C., Li, Z., Zhang, L., & Xie, J. (2020). Paleomagnetism of middle Triassic lavas from northern Qiangtang (Tibet): Constraints on the closure of the Paleo-Tethys ocean. *Journal of Geophysical Research: Solid Earth*, *125*(2), e2019JB017804. https://doi.org/10.1029/2019jb017804

Sun, W. D., Lin, C. T., Zhang, L. P., Liao, R. Q., & Li, C. Y. (2018). The formation of the South China Sea resulted from the closure of the Neo-Tethys: A perspective from regional geology. *Acta Petrologica Sinica*, *34*(12), 3467–3478.

Sun, W. D., Liu, L. J., Hu, Y. B., Ding, W., Liu, J. Q., Ling, M. X., et al. (2018). Post-ridge-subduction acceleration of the Indian plate induced by slab rollback. *Solid Earth Sciences*, *3*(1), 1–7. https://doi.org/10.1016/j.sesci.2017.12.003

Sun, Z., Jiang, W., Li, H., Pei, J., & Zhu, Z. (2010). New paleomagnetic results of Paleocene volcanic rocks from the Lhasa block: Tectonic implications for the collision of India and Asia. *Tectonophysics*, *490*(3–4), 257–266. https://doi.org/10.1016/j.tecto.2010.05.011

Sun, Z., Pei, J., Li, H., Xu, W., Jiang, W., Zhu, Z., et al. (2012). Palaeomagnetism of late Cretaceous sediments from southern Tibet: Evidence for the consistent palaeolatitudes of the southern margin of Eurasia prior to the collision with India. *Gondwana Research*, *21*(1), 53–63. https://doi.org/10.1016/j.gr.2011.08.003

Sun, Z. M., Yang, Z. Y., Pei, J. L., Yang, T. S., & Wang, X. S. (2006). New Early Cretaceous paleomagnetic data from volcanic and red beds of the eastern Qaidam Block and its implications for tectonics of Central Asia. *Earth and Planetary Science Letters*, *243*(1–2), 268–281. https://doi.org/10.1016/j.epsl.2005.12.016

Sundell, K. E., Laskowski, A. K., Kapp, P. A., Ducea, M. N., & Chapman, J. B. (2021). Jurassic to Neogene Quantitative crustal Thickness estimates in southern Tibet. *Geological Society of America Today*, *31*(6), 4–10. https://doi.org/10.1130/GSATG461A.1

Tan, X., Gilder, S., Kodama, K. P., Jiang, W., Han, Y., Zhang, H., et al. (2010). New paleomagnetic results from the Lhasa block: Revised estimation of latitudinal shortening across Tibet and implications for dating the India-Asia collision. *Earth and Planetary Science Letters*, *293*(3–4), 396–404. https://doi.org/10.1016/j.epsl.2010.03.013

Tang, X. D., Huang, B. C., Yang, L. K., Yi, Z. Y., Qiao, Q. Q., & Chen, L. W. (2013). Paleomagnetism and Ar-Ar geochronology of Cretaceous volcanic rocks in the middle Lhasa terrane, China and tectonic implications. *Chinese Journal of Geophysics-Chinese Edition*, *56*(1), 136–149. https://doi.org/10.6038/cjg20130114

Tong, Y., Yang, Z., Pei, J., Wang, H., Xu, Y., & Pu, Z. (2017). Paleomagnetism of the Upper Cretaceous red-beds from the eastern edge of the Lhasa terrane: New constraints on the onset of the India-Eurasia collision and latitudinal crustal shortening in southern Eurasia. *Gondwana Research*, *48*, 86–100. https://doi.org/10.1016/j.gr.2017.04.018

Tong, Y. B., Yang, Z. Y., Li, J. F., Pei, J. L., & Li, J. F. (2019). New insights into the collision process of India and Eurasia: Evidence from the syntectonic-sedimentation-induced inclinational divergence of Cretaceous paleomagnetic data of the Lhasa Terrane. *Earth-Science Reviews*, *190*, 570–588. https://doi.org/10.1016/j.earscirev.2019.02.009

Torsvik, T. H., Van derVoo, R., Preeden, U., Mac Niocaill, C., Steinberger, B., Doubrovine, P. V., et al. (2012). Phanerozoic polar wander, palaeogeography and dynamics. *Earth-Science Reviews*, *114*(3–4), 325–368. https://doi.org/10.1016/j.earscirev.2012.06.007

Van der Voo, R. (1990). The reliability of paleomagnetic data. *Tectonophysics*, *184*(1), 1–9. https://doi.org/10.1016/0040-1951(90)90116-p

Van der Voo, R., van Hinsbergen, D. J., Domeier, M., Spakman, W., & Torsvik, T. H. (2015). Latest Jurassic–earliest Cretaceous closure of the Mongol-Okhotsk Ocean: A paleomagnetic and seismological-tomographic analysis. *Geological Society of America Special Papers*, *513*, 589–606. https://doi.org/10.1130/2015.2513(19)

Van Hinsbergen, D. J. J., Lippert, P. C., Dupont-Nivet, G., McQuarrie, N., Doubrovine, P. V., Spakman, W., & Torsvik, T. H. (2012). Greater India Basin hypothesis and a two-stage Cenozoic collision between India and Asia. *Proceedings of the National Academy of Sciences of the United States of America*, *109*(20), 7659–7664. https://doi.org/10.1073/pnas.1117262109

Van Hinsbergen, D. J. J., Steinberger, B., Doubrovine, P. V., & Gassmoeller, R. (2011). Acceleration and deceleration of India-Asia convergence since the Cretaceous: Roles of mantle plumes and continental collision. *Journal of Geophysical Research: Solid Earth*, *116*(B6), B06101. https://doi.org/10.1029/2010jb008051

Wan, B., Wu, F. Y., Chen, L., Zhao, L., Liang, X. F., Xiao, W. J., & Zhu, R. X. (2019). Cyclical one-way continental rupture-drift in the Tethyan evolution: Subduction-driven plate tectonics. *Science China Earth Sciences*, *62*(12), 2005–2016. https://doi.org/10.1007/s11430-019-9393-4

Wang, C., Ding, L., Zhang, L. Y., Kapp, P., Pullen, A., & Yue, Y. H. (2016). Petrogenesis of Middle-Late Triassic volcanic rocks from the Gangdese belt, southern Lhasa terrane: Implications for early subduction of Neo-Tethyan oceanic lithosphere. *Lithos*, *262*, 320–333. https://doi.org/10.1016/j.lithos.2016.07.021

Wang, J., Wang, Q., Zhang, C., Dan, W., Qi, Y., Zhang, X. Z., & Xia, X. P. (2018). Late Permian Bimodal volcanic rocks in the northern Qiangtang terrane, central Tibet: Evidence for interaction between the Emeishan plume and the Paleo-Tethyan subduction system. *Journal of Geophysical Research: Solid Earth*, *123*(8), 6540–6561. https://doi.org/10.1029/2018jb015568

Wang, S., Yang, T., Gao, F., Bian, W., Jin, J., Peng, W., et al. (2022). Paleomagnetic and geochronological results of the Risong Formation in the Western Lhasa terrane: Insights into the Lhasa-Qiangtang collision and stratal age. *Palaeogeography, Palaeoclimatology, Palaeoecology*, *586*, 110778. https://doi.org/10.1016/j.palaeo.2021.110778

Wang, X. D., Hu, K. Y., Shi, Y. K., Chen, J. T., Yang, S. R., Ye, X. Y., et al. (2021). The missing upper Carboniferous in the Cimmerian continent: A critical review. *Earth-Science Reviews*, *217*, 103627. https://doi.org/10.1016/j.earscirev.2021.103627

Wei, B. T., Cheng, X., Domeier, M., Jiang, N., Wu, Y. Y., Zhang, W. J., et al. (2022). Placing Another Piece of the Tethyan Puzzle: The first Paleozoic paleomagnetic data from the South Qiangtang block and its paleogeographic implications. *Tectonics*, *41*(10), e2022TC007355. https://doi.org/10.1029/2022tc007355

Yang, T., Jin, J., Bian, W., Ma, Y., Gao, F., Peng, W., et al. (2019). Precollisionallatitude of the northern Tethyan Himalaya from the Paleocene redbeds and its implication for greater India and the India-Asia collision. *Journal of Geophysical Research: Solid Earth*, *124*(11), 10777–10798. https://doi.org/10.1029/2019JB017927

Yang, T., Ma, Y., Bian, W., Jin, J., Zhang, S., Wu, H., et al. (2015). Paleomagnetic results from the early Cretaceous Lakang formation lavas: Constraints on the paleolatitude of the Tethyan Himalaya and the India-Asia collision. *Earth and Planetary Science Letters*, *428*, 120–133. https://doi.org/10.1016/j.epsl.2015.07.040

Yang, T., Ma, Y., Zhang, S., Bian, W., Yang, Z., Wu, H., et al. (2015). New insights into the India-Asia collision process from Cretaceous paleomagnetic and geochronologic results in the Lhasa terrane. *Gondwana Research*, *28*(2), 625–641. https://doi.org/10.1016/j.gr.2014.06.010

Yan, M., Zhang, D., Fang, X., Ren, H., Zhang, W., Zan, J., et al. (2016). Paleomagnetic data bearing on the Mesozoic deformation of the Qiangtang block: Implications for the evolution of the Paleo- and Meso-Tethys. *Gondwana Research*, *39*, 292–316. https://doi.org/10.1016/j.gr.2016.01.012

Yi, Z., Huang, B., Yang, L., Tang, X., Yan, Y., Qiao, Q., et al. (2015). A quasi-linear structure of the southern margin of Eurasia prior to the India-Asia collision: First paleomagnetic constraints from Upper Cretaceous volcanic rocks near the Western syntaxis of Tibet. *Tectonics*, *34*(7), 1431–1451. https://doi.org/10.1002/2014tc003571

Yi, Z., Liu, Y., & Meert, J. G. (2019). A true polar wander trigger for the Great Jurassic East Asian Aridification. *Geology*, *47*(12), 1112–1116. https://doi.org/10.1130/G46641.1

Yi, Z. Y., Huang, B. C., Chen, J. S., Chen, L. W., & Wang, H. L. (2011). Paleomagnetism of early Paleogene marine sediments in southern Tibet, China: Implications to onset of the India-Asia collision and size of Greater India. *Earth and Planetary Science Letters*, *309*(1–2), 153–165. https://doi.org/10.1016/j.epsl.2011.07.001

Yi, Z. Y., Wang, T. Y., Meert, J. G., Zhao, Q., & Liu, Y. S. (2021). An initial collision of India and Asia in the equatorial Humid belt. *Geophysical Research Letters*, *48*(9), e2021GL093408. https://doi.org/10.1029/2021gl093408

Yin, A., & Harrison, T. M. (2000). Geologic evolution of the Himalayan-Tibetan orogen. *Annual Review of Earth and Planetary Sciences*, *28*(1), 211–280. https://doi.org/10.1146/annurev.earth.28.1.211

Yu, L., Yan, M. D., Domeier, M., Guan, C., Shen, M. M., Fu, Q., et al. (2022). New paleomagnetic and Chronological constraints on the late Triassic position of the eastern Qiangtang terrane: Implications for the closure of the Paleo-Jinshajiang ocean. *Geophysical Research Letters*, *49*(2), e2021GL096902. https://doi.org/10.1029/2021gl096902

Yuan, J., Deng, C., Yang, Z., Krijgsman, W., ThubtantseringQin, H., Shen, Z., et al. (2022). Triple-stage India-Asia collision involving arc-continent collision and subsequent two-stage continent-continent collision. *Global and Planetary Change*, *212*, 103821. https://doi.org/10.1016/j.gloplacha.2022.103821

Yuan, J., Yang, Z. Y., Deng, C. L., Krijgsman, W., Hu, X. M., Li, S. H., et al. (2021). Rapid drift of the Tethyan Himalaya terrane before two-stage India-Asia collision. *National Science Review*, *8*(7), nwaa173. https://doi.org/10.1093/nsr/nwaa173

Zahirovic, S., Matthews, K. J., Flament, N., Muller, R. D., Hill, K. C., Seton, M., & Gurnis, M. (2016). Tectonic evolution and deep mantle structure of the eastern Tethys since the latest Jurassic. *Earth-Science Reviews*, *162*, 293–337. https://doi.org/10.1016/j.earscirev.2016.09.005

Zhang, C., Liu, C. Z., Xu, Y., Ji, W. B., Wang, J. M., Wu, F. Y., et al. (2019). Subduction re-initiation at dying ridge of Neo-Tethys: Insights from mafic and metamafic rocks in Lhaze ophiolitic melange, Yarlung-Tsangbo Suture Zone. *Earth and Planetary Science Letters*, *523*, 115707. https://doi.org/10.1016/j.epsl.2019.07.009

Zhang, Y. C., Shi, G. R., & Shen, S. Z. (2013). A review of Permian stratigraphy, palaeobiogeography and palaeogeography of the Qinghai-Tibet Plateau. *Gondwana Research*, *24*(1), 55–76. https://doi.org/10.1016/j.gr.2012.06.010

Zhou, Y., Cheng, X., Yu, L., Yang, X., Su, H., Peng, X., et al. (2016). Paleomagnetic study on the Triassic rocks from the Lhasa terrane, Tibet, and its paleogeographic implications. *Journal of Asian Earth Sciences*, *121*, 108–119. https://doi.org/10.1016/j.jseaes.2016.02.006

Zhu, D. C., Li, S. M., Cawood, P. A., Wang, Q., Zhao, Z. D., Liu, S. A., & Wang, L. Q. (2016). Assembly of the Lhasa and Qiangtang terranes in central Tibet by divergent double subduction. *Lithos*, *245*, 7–17. https://doi.org/10.1016/j.lithos.2015.06.023

References From the Supporting Information

Cogné, J. P. (2003). PaleoMac: A Macintosh (TM) application for treating paleomagnetic data and making plate reconstructions. *Geochemistry, Geophysics, Geosystems*, *4*(1), 1007. https://doi.org/10.1029/2001gc000227

Enkin, R. J., & A Computer Program Package for Analysis and Presentation of Paleomagnetic Data. (1994). *Pacific Geoscience Centre*. Geological Survey of Canada.

Fisher, R. (1953). Dispersion on a sphere. *Proceedings of the Royal Society of London Series a-Mathematical and Physical Sciences*, *217*(1130), 295–305. https://doi.org/10.1098/rspa.1953.0064

Gerritsen, D., Vaes, B., & van Hinsbergen, D. J. (2022). Influence of data filters on the position and precision of paleomagnetic poles: What is the optimal sampling strategy? *Geochemistry, Geophysics, Geosystems*, *23*(4), e2021GC010269. https://doi.org/10.1029/2021GC010269

Lin, J., Liu, Y., Yang, Y., & Hu, Z. (2016). Calibration and correction of LA-ICP-MS and LA-MC-ICP-MS analyses for element contents and isotopic ratios. *Solid Earth Sciences*, *1*(1), 5–27. https://doi.org/10.1016/j.sesci.2016.04.002

Liu, Y. S., Hu, Z. C., Gao, S., Gunther, D., Xu, J., Gao, C. G., & Chen, H. H. (2008). In situ analysis of major and trace elements of anhydrous minerals by LA-ICP-MS without applying an internal standard. *Chemical Geology*, *257*(1–2), 34–43. https://doi.org/10.1016/j.chemgeo.2008.08.004

Maxbauer, D. P., Feinberg, J. M., & Fox, D. L. (2016). Max UnMix: A web application for unmixing magnetic coercivity distributions. *Computers & Geosciences*, *95*, 140–145. https://doi.org/10.1016/j.cageo.2016.07.009

Paterson, G. A., Zhao, X., Jackson, M., & Heslop, D. (2018). Measuring, Processing, and Analyzing hysteresis data. *Geochemistry, Geophysics, Geosystems*, *19*(7), 1925–1945. https://doi.org/10.1029/2018GC007620